UNIVERSITÀ DEGLI STUDI DI GENOVA

Dipartimento di Fisica

PhD Thesis

Charm jet identification performance for the ATLAS experiment and development of future tracking detectors

Supervisor:
Prof. C. Schiavi

Candidate:
Dr. A. Lapertosa

Referees:
Dr. A. Chisholm
Dr. F. Sforza

26 March 2019

Abstract

ATLAS is a particle physics experiment at the Large Hadron Collider (LHC) operating at the CERN laboratory in Geneva. ATLAS is designed to be a general purpose detector: rather than focusing on a particular physical process, it can measure an entire range of signals in order to study many phenomena and search for new particles that could emerge from LHC collisions. During the course of my Ph.D. program, I contributed to several different activities in the context of the ATLAS experiment: from data taking to public outreach, including data quality assessment, b-tagging performance measurement, standard model physics measurement, test beam with detector components and R&D on silicon wafers in view of future tracking detectors. In this thesis, I will mainly focus on the measurement of the charm jet indentification performance by specialized b-tagging algorithms, which has been my main contribution, and on the test beam experiments performed on pixel detector modules with unprecendented high energy and intensity proton beam, for beam-loss scenario studies.

Contents

Introduction

In this thesis, several contribution I made to the ATLAS experiment are described, ranging from data taking to public outreach activities. ATLAS is a multi purpose experiment located at the Large Hadron Collider (LHC) operating at the CERN laboratory in Geneva. The ATLAS collaboration is made by more than 3000 physicists coming from 38 different countries. The ATLAS detector was designed to measure a wide range of signals, in order to study many different physical processes and potentially discover new particles.

When I joined the ATLAS collaboration, in Spring 2015, the ATLAS detector was fully operational and the Run 2 data taking was about to start. In such a context, one could imagine that the only possibility to contribute to an already built and operational experiment would be to perform data analysis. From my experience, this is not completely true: there are different fields that can be explored.

During my master degree thesis and along the three years of the Ph.D. program, I had the possibility to contribute to many activities in the context of the ATLAS experiment, with different degrees of commitment. In the meanwhile, the experiment has gone through 4 years of operations (Run 2: 2015-2018) along with the other LHC experiments. The data taking ended in December 2018 with the completion of the Run 2 physics program and the start of a two-years shutdown of the accelerator facilities (Long Shutdown 2). In 2021, the physics program will resume with Run 3, then the LHC should conclude the first part of its physics program at the end of 2023 with an expected integrated luminosity of proton-proton collisions of 300 fb^{-1}. During Long Shutdown 3 the LHC accelerator will be upgraded to achieve a higher instantaneous luminosity: the era of the High-Luminosity LHC (HL-LHC) will start. The ATLAS detector will be upgraded too, in order to cope with the HL-LHC environment. In particular, the tracking system, which has the purpose of reconstructing tracks and vertices, will be completely replaced by a new silicon detector with increased granularity and radiation hardness: the Inner Tracker (ITk).

Beyond the activities related to the current operation of the ATLAS experiment (i.e. detector operations, combined performance, data analysis), I have been involved in laboratory activities focusing on the future tracking system upgrade. The ATLAS Genoa group has a long tradition in silicon detector production and assembly and is going to take part in the ITk detector construction. The building block of the typical silicon detector, the modules, are built assembling silicon tiles (sensor and

microelectronic chip tiles). The tiles are produced by foundries in form of thin round slices (wafers), then the individual componets are separated. I contributed to the R&D phase of the Wafer Level Packaging technology, a process developed with the goal of rebuilding a wafer structure starting from previously diced tiles. I performed measurements to assess the quality of the rebuilt wafers and then compared the results with the technical specifications of silicon detector components to be used for high energy physics application (i.e. the ITk pixel detector). Six wafers were produced with this technique by MicroFab Solutions in Trento within the AIDA-2020 framework activities. AIDA-2020 (Advanced European Infrastructures for Detectors at Accelerators) is an European project with the aim of innovating detector technologies and improving testing infrastractures. It is a unique project with a broad field of applications: not only the developement of innovative components for future detectors, but also for the upgrade plans of the current detectors. The process flow of the Wafer Level Packaging technique is described in this thesis, together with the results of the measurements of the wafers properties (Chapter 4).

Moreover, I took part in two test beam campaigns at the CERN HiRadMat (High Radiation to Materials) facility. In this experiments, strip and pixel silicon detector modules have been exposed to an unprecedented high energy and intensity proton beam to study the performance degradation of real detector components in case of beam-loss scenarios. In case of a beam-loss event, the particles that make up the beam are deviated from their expected trajectory: a large cascade of particles, from the interaction of the beam with the surrounding material, may hit the detectors. After the accelerator upgrade, the aperture of the HL-LHC quadrupoles in the proximity of the interaction regions will be larger with respect to the current LHC aperture, reducing in this way the shielding potential of this material. The increased intensity of the collisions produced by the HL-LHC accelerator, together with the larger apertures, requires for the measurement of the beam-loss survival threshold of the tracking detector components, both sensors and electronics. After an introduction to the HiRadMat facility, the experimental setup and the beam operations are described, along with the results (Chapter 5).

The ATLAS experiment has a long and wide experience in the data quality assessment, obtained after years of operations, which has guaranteed many successful physics results. The data quality software is continuosly updated in order to be ready to assess the quality of the data in any condition: standard proton-proton collisions, high luminosity collisions, low luminosity collisions, special runs, heavy ion collisions. Within this frame, I contributed to the b-tagging data quality software updates during 2018 data taking. The term "b-tagging" collectively describes the tools developed to identify jets generated from the hadronization of the beauty quarks (b-jets). The correct identification is of fundamental importance for the physics analyses involving b-jets in the final state: top quark and Higgs boson studies, as well as the search for new physics phenomena beyond the Standard Model. With the experience gained in the software updates, I acted as b-tagging data quality ex-

pert, helping in following up the issues and in the organizational aspects of the data quality shifts. After a brief introduction to vertex, tracks and jet reconstruction, the ATLAS b-tagging algorithms are presented (Chapter 7). Thereafter, the ATLAS data quality software is introduced, focusing on b-tagging tools. A detailed description of the improvements to the b-tagging monitoring tools is presented (Chapter 8), along with few examples of relevant issues encountered during 2018 data taking.

As said before, the analysis of the data collected during Run 2 operations was not the only activity I was involved in, but it was my very first contribution to the ATLAS experiment and it is the main part of this thesis (Chapter 10): the measurement of the b-tagging performance on a charm jet sample. The performance of the b-tagging algorithms is calibrated on data, measuring the efficiency to tag a jet originated from a b quark (b-jet tagging efficiency) as a b-jet or to mistakenly tag a jet originated from a charm quark (c-jet tagging efficiency) or from a light quark or a gluon (mistag rate). The c-jet tagging efficiency was measured by the ATLAS experiment with different techniques: the D^*, W+c and $t\bar{t}$ methods (Chapter 9). This thesis work focuses on the W+c method, based on a sample of c-jets produced in association with a W boson, with the c-jet identified by a soft muon coming from a semileptonic c-hadron decay. I used this method to measure the c-jet tagging efficiency of the Run 2 b-tagging algorithms (Chapter 10) on 36 fb^{-1} of proton-proton collision data collected at $\sqrt{s} = 13$ TeV by the ATLAS experiment. The same measurement is performed on simulated event samples, then a data-to-simulation scale factor is derived, defined as the ratio of the efficiency on data over the efficiency on simulated event samples. The data-to-simulation scale factors measured on W+c events are finally combined with the results of the measurements performed on $t\bar{t}$ events to reduce total uncertainties.

I am exploiting the experience gained during the measurement of the b-tagging efficiency with a W+c sample to measure the production cross section of this process. The $pp \to WcX$ production is dominated by the $gs \to Wc$ process, therefore this measurement is directly sensitive to the s-quark distribution function in the proton at momentum-transfer values on the order of the W-boson mass. The first steps of the measurement of the production of a W boson in association with a single charm quark using 140 fb^{-1} of proton-proton collision data at $\sqrt{s} = 13$ TeV collected with the ATLAS detector at the LHC from 2015 to 2018 are presented (Chapter 11). The events are selected similarly to what done for the b-tagging efficiency measurement, with significant improvements in the statistics, as both electron and muon W-boson decay channels are explored in this measurement.

Finally, during 2018, I contributed to the data taking operations of the ATLAS experiment, taking shifts in the ATLAS Control Room at the Inner Detector desk. I partecipated as well to outreach activities, in particular to the Genoa Science Festival, which is one of the main science fairs in Italy. Few hints on these activities can be found in Bonus Chapters 6 and 12, respectively.

Chapter 1

The ATLAS experiment at LHC

More than 60 years ago, 12 European countries founded CERN (originally "Conseil Européen pour la Recherche Nucleaire") to promote international cooperation on scientific research. In the following years, CERN laboratories, based on the particle accelerator technology, addressed many questions and led the scientific community torward the understanding of the atomic, nuclear and sub-nuclear physics. Nowadays, CERN is an intergovernmental organization employing around 2500 people among physicists, engineers, technichians and administratives in its laboratories builded on the border between France and Switzerland. More than 10000 scientists from all over the world operate with its facilities, making the CERN one of the world largest centers for scientific research.

The energy required to study more and more in deep the fundamental constituents of matter often required the building of a new generation of high-energy accelerators. Currently, these accelerators are the constituents of a unique complex (see Figure 1.1), capable of increasing the speed and consequently the energy of a wide range of particles, such as protons, antiprotons, electrons and ions. At the top stage of this accelerator complex stands the Large Hadron Collider: currently the most powerful accelerator in the world.

1.1 Large Hadron Collider at CERN

The Large Hadron Collider (LHC) [1, 2] accelerate particles along their trajectory, in the same tunnel once containing the Large Electron-Positron Collider (LEP) [3]. Within the LHC 27 km length, more than 1200 superconducting dipoles are connected together and cooled at 1.9 K by liquid helium. These magnets generate a 8 T magnetic field that bends the beams along their circular track. Almost 400 quadrupole magnets are used to guide and focus the beams, providing the beams with small transverse sections. Radiofrequency cavities are used to accelerate the beams until they reach the desired energy. LHC accelerates protons or ions to perform collisions at the TeV energy scale, allowing physicists to test the theoretical

predictions of many proposed particle physics models.

After the dismantling of LEP, in the period going from 2000 to 2008, the LHC was built in the tunnel at about 100 m underground. The counter-rotating beams collide at the 4 interaction points, where the ATLAS, ALICE, CMS and LHCb experiments are placed. After accelerator commissioning and cosmic rays studies, LHC begun operations on 10 September 2008. An accidental liquid helium leak due to a broken connection between two magnets caused a long stop to repair more than 50 damaged magnets. After 14 months, the LHC was back in November 2009 with particle collisions at the record energy of $\sqrt{s} = 2.36$ TeV in the center of mass. The energy was then increased in 2011 ($\sqrt{s} = 7$ TeV) and again in 2012 ($\sqrt{s} = 8$ TeV). From September 2013 to March 2015, the LHC underwent the first Long Shutdown: in these months the magnet connections were renewed to get stronger for the new energy level. The LHC resumed operations in April 2015, with both beams circulating at 6.5 GeV energy. In the following years, LHC delivered collisions at the record energy of $\sqrt{s} = 13$ TeV in the center of mass, becoming once again the most powerful accelerator of the world. LHC operated until the end of 2018, when the second Long Shutdown is started.

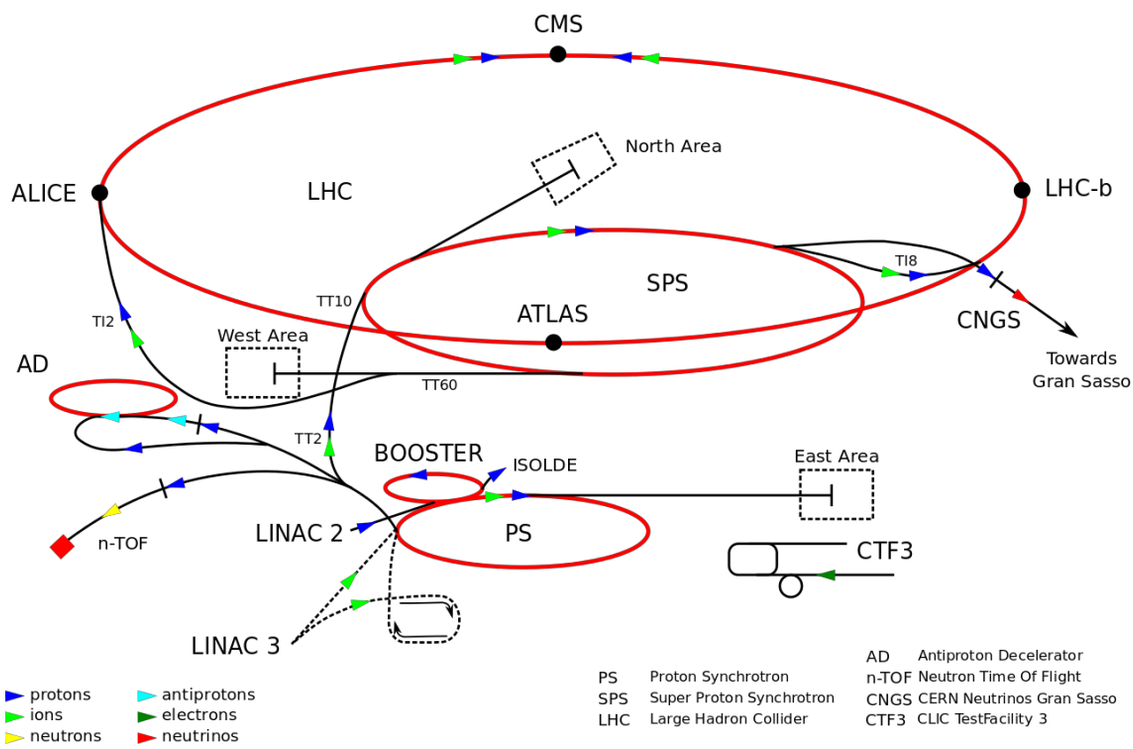

Figure 1.1: CERN accelerator complex: LINAC 2, BOOSTER, PS and SPS operate in the pre-acceleration chain of the LHC. They also accelerate different beams for a wide range of physics experiments: test beams, AD, n-TOF, ISOLDE, CNGS.

Before entering the LHC, the protons extracted from an hydrogen source go through an acceleration chain composed by many stages (see Figure 1.1):

- LINear ACcelerator 2 (LINAC 2): a 36 m long linear accelerator initially increases the energy up to 50 MeV;
- Booster (BOOSTER): four superimposed rings with a 25 m diameter accelerates the protons up to 1.4 GeV;
- Proton Synchrotron (PS): a 628 m long circular accelerator composes bunches of protons and brings them up to 26 GeV;
- Super Proton Synchrotron (SPS): a 2 km diameter ring accelerates the beams up to 450 GeV, before injecting them into LHC.

During the second Long Shutdown, LINAC 2 will be replaced by LINAC 4, a 80 long linear accelerator that will bring protons up to 160 MeV. Booster an PS will be replaced too, by Superconducting Proton Linac and by PS2: these upgrades are the only possible way to reach a higher luminosity level (see Equation 1.1).

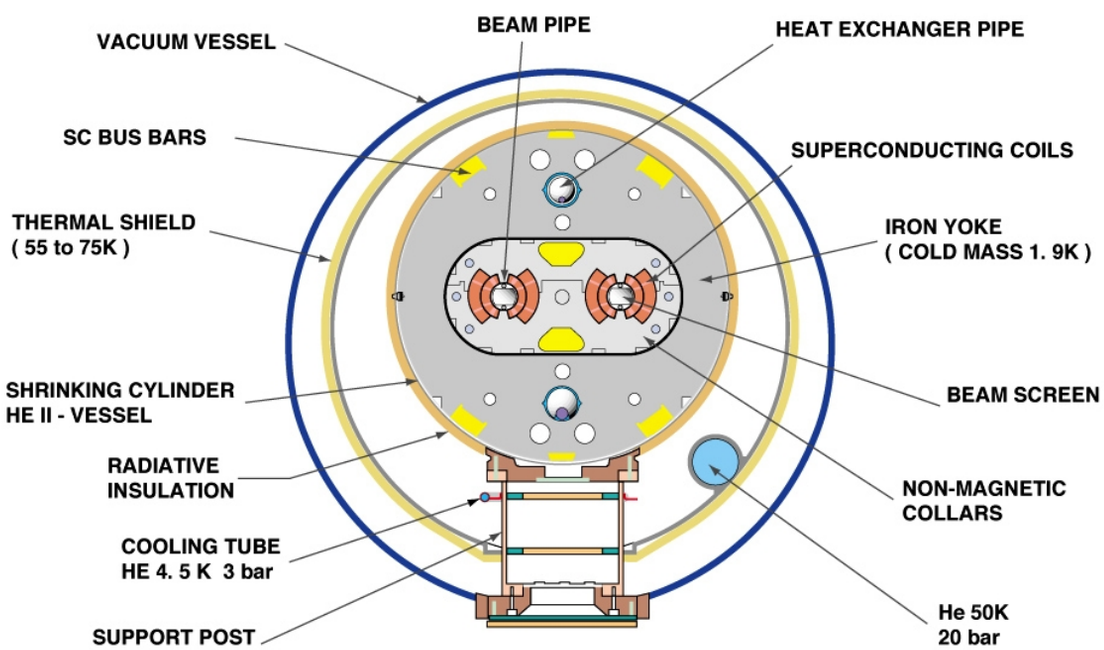

Figure 1.2: Section view of the magnetic dipole of LHC.

Two counter-rotating beams (made by protons or ions) circulate in two separate vacuum chambers contained in a single beam pipe (see Figure 1.2). Each beam is composed by many tiny little bunches of particles (a maximum of 2808 bunches, each one made by about 10^{11} protons). It takes 4 minutes and 20 seconds to accelerate enough protons to fill each LHC ring, then several minutes are needed to reach the final LHC energy. Beams at the extablished energy circulate for 10 hours or more into LHC, colliding at a rate of 40 MHz (one bunch-crossing event per 25 ns) until the number of protons runs out. Then the beams are dumped, the magnets are

ramped down, the whole system goes through ∼30 minutes of rest and a new cycle begins.

The variable describing the collider ability to produce collisions is the instantaneous luminosity, defined as:

$$\mathcal{L} = f n_p \frac{\mathrm{N_1 N_2}}{4\pi\sigma_x\sigma_y} \tag{1.1}$$

where σ_x and σ_y represent the gaussian transverse profiles of the beams, $\mathrm{N_1}$ and $\mathrm{N_2}$ represents the number of protons in the bunch, f is the revolution frequence of the bunches and n_p is the number of bunches in the beam. To increase the rate of interesting events, the number of collisions needs to be increased. This could be obtained in different ways: increasing the number of bunches in the beam, increasing the number of protons in each bunch, increasing the revolution frequency of the bunches, reducing the transverse sections of the beams.

The number of expected events n for a process having cross section σ is:

$$n = L\ \sigma, \tag{1.2}$$

where L is the integrated luminosity, defined as the integral of the instantaneous luminosity $\mathcal{L}$ in the time interval from t_1 to t_2:

$$L = \int_{t_1}^{t_2} \mathcal{L}\ dt. \tag{1.3}$$

After reaching the final energy, the beams collide in four experimental areas where the particle detectors of the main LHC experiments stand:

- A Large Ion Collider Experiment (ALICE): an experiment with the specific purpose of studing the quark-gluon plasma physics through ion-ion collisions, in order to gain further knowledge on the state of the matter at extreme energy density;

- A Toroidal LHC ApparatuS (ATLAS): a glimpse into the ATLAS experiment physics program is provided in Section 1.4;

- Compact Muon Solenoid (CMS): a general purpose experiment with many different goals as Higgs boson studies, Super Symmetry and Dark Matter searches;

- Large Hadron Collider beauty (LHCb): an experiment focused on beauty physics, aiming toward a better understanding of the rare B hadrons phenomena and a precise measurement of the CP violation parameters.

1.2 Standard Model theory

Nowadays, the most satisfying theory describing particle interaction is the Standard Model (SM) [4–6], born after a century of deep studies over the fundamental constituents of matter. The SM describes the electromagnetic, weak and strong interactions in terms of fields, bringing together the electro-weak theory (also referred as Glashow-Weinberg-Salam Theory) and the Quantum Chromo-Dynamics (QCD). The gravitational interaction is not included in this model: it dominates in the universe on a large scale, but it is not easy to describe it along with SM in terms of a quantum-relativistic field theory. From the theoretical point of view, the Standard Model is a gauge theory based on the symmetry group:

$$U(1) \otimes SU(2) \otimes SU(3) \tag{1.4}$$

where $U(1) \otimes SU(2)$ is the group of unified weak and electromagnetic interactions and SU(3) is the group associated to strong interaction. The interactions are exchanged by means of "messenger particles", the gauge bosons: the photons (electromagnetic interaction), the gluons (strong interaction) and $W^{\pm}$ and Z^0 bosons (weak interaction).

Gauge Boson	Mass [GeV]	Interaction	Range [m]
gluon (g)	0	Strong	10^{-15}
photon (γ)	0	Electromagnetic	∞
$W^{\pm}$	80.4	Weak	10^{-17}
Z^0	91.2	Weak	10^{-17}

Table 1.1: Gauge bosons are mediators of the Strong, Electromagnetic and Weak Interactions. The experimentally measured masses are reported, along with the effective ranges of the interactions.

According to the Standard Model, there are few fundamental particles divided in two main classes: 12 fermions with spin 1/2 (6 leptons and 6 quarks) and 5 bosons with spin 1 (actually, 8 different gluons exist, from the properties of the SU(3) symmetry). Of the three forces, only the weak force affects all fermions; the electromagnetic force is felt only by the charged particles, while only the quarks interact via the strong force.

	Generation			
	I	II	III	Electric charge
Leptons	$\begin{pmatrix} \nu_e \\ e^- \end{pmatrix}$	$\begin{pmatrix} \nu_\mu \\ \mu^- \end{pmatrix}$	$\begin{pmatrix} \nu_\tau \\ \tau^- \end{pmatrix}$	$\begin{matrix} 0 \\ -1 \end{matrix}$
Quarks	$\begin{pmatrix} u \\ d \end{pmatrix}$	$\begin{pmatrix} \mathrm{c} \\ s \end{pmatrix}$	$\begin{pmatrix} t \\ \mathrm{b} \end{pmatrix}$	$\begin{matrix} 2/3 \\ -1/3 \end{matrix}$

Table 1.2: Leptons and quarks: I, II and III generation.

Lepton	Mass		Quark	Mass
ν_e	< 2 eV		u	2.3 MeV
e^-	0.511 MeV		d	4.8 MeV
ν_μ	< 0.19 MeV		c	1.3 GeV
μ^-	105.7 MeV		s	95 MeV
ν_τ	< 18.2 MeV		t	173 GeV
τ^-	1776.8 MeV		b	4.2 GeV

Table 1.3: Leptons and quarks measured masses.

Since the electroweak theory describes massless fermions and gauge bosons, while evidence tells us that many particles have mass, new parts have to be added to the theory to solve this puzzle: the spontaneous symmetry breaking of the electroweak gauge symmetry and the Higgs mechanism. This introduces a new particle into the theory: the Higgs boson. Since the theory can only indirectly predict favored values for the Higgs boson mass, a long search has been performed at the highest energy colliders: LEP (electron-positron collisions, up to 200 GeV), Tevatron (proton-antiproton collisions, up to 1.96 TeV) and LHC (proton-proton collisions, up to 13 TeV). Finally, the Higgs boson have been discovered: this success opens the field to the era of precision measurements of its properties (further details in Section 1.4.1).

1.3 QCD and PDFs

Proton-proton collisions are well understood and described as parton interactions within the QCD theory. According to the QCD theory, the partons (quarks and gluons) are coloured states that can not exist individually. The quarks usually combine to form colourless states: pairs of quarks-antiquarks bound together (mesons) and triplets of differently coloured quarks or antiquarks (barions). This is the reason why free quarks and gluons always undergo a hadronization process: other quarks and gluons are generated in the so-called "parton shower", then a tight cone of hadrons (jet) emerges. It is impossible to detect free quarks before the hadronization (except for indirect measurements of the the top quark, which decays before hadronizing because of its very large mass), but it is still possible to identify the quark from which the jet originated.

Jets can be divided in three main categories (flavours): b-jets originating from a beauty quark; c-jets from a charm quark or light jets from a gluon or a up, down or strange quark. The correct identification of jets containing b hadrons (hence b-tagging) is of capital importance for many physics analyses: for top quark studies and Higgs measurements, as well as the search for new physics fenomena beyond Standard Model.

Experimental evidence tell us that the protons are bound states of two up and one down quark (valence quarks) which exchange gluons. In addition there are quark-

antiquark pairs of any flavour which are generated from emitted gluons (sea quarks). Inside the proton, each parton carries a fraction x of the proton momentum. The Parton Density Functions (PDFs) describes the probabilities for a parton to carry a certain momentum fraction in interactions with a given transferred momentum Q^2: $f(x, Q^2)$.

In Figure 1.3, the proton PDFs and their uncertainties (before the LHC era) are shown: for high x values the valence quarks are dominating, while at low x the sea quarks are giving a relevant contribution. For high values of the transferred momentum, the sea quarks contribution is enhanced. Results from many experiments are combined together as inputs to extract the PDFs: fitting collaborations are providing parametrisations of the PDFs for each of the quark flavours. The LHC experiments have contributed with many studies to improve the PDFs knowkledge and understanding [7], reducing uncertainties. The s quark PDF, of particular interest for this thesis, is currently poorly constrained by direct experimental measurements, especially at low Q^2.

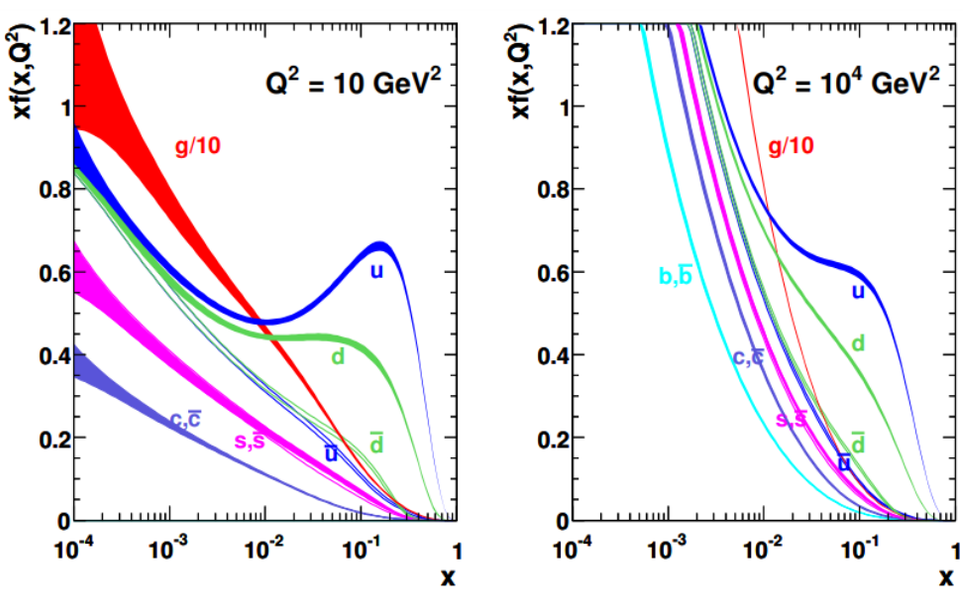

Figure 1.3: Parametrization of the proton PDFs [8] for different momentum transfers.

1.4 ATLAS physics highlights

ATLAS [9] is a multi purpose experiment located at the Interacting Point 1 (IP1) into the LHC tunnel. The ATLAS collaboration is made by more than 3000 physicist coming from 38 different countries. The ATLAS experiment was firstly proposed in 1992, then in 1999 a Tecnical Design Report [10] was defined. The detector assembly was completed in 2008, the physics program started with Run 1 (2011-2012) then a detector upgrade was performed during Long Shutdown 1 (2013-2014) and physics

Run 2 followed (2015-2018). Right now the detector is under maintenance, during Long Shutdown 2 (2019-2020). The physics program will resume in 2021, with Run 3.

During Run 2 operations, the LHC collisions doubled the design instantaneous luminosity, with ATLAS reaching $\mathcal{L} = 2.14 \cdot 10^{34}\ cm^{-2}s^{-1}$ and mean pile-up values up to 70 (Figure 1.4, right). The total amount of good data for physics analyses collected by the ATLAS detector during Run 2, measured in terms of integrated luminosity L, reaches 140 fb^{-1} (Figure 1.4, left), allowing to study rare phenomena characterized by very low cross section.

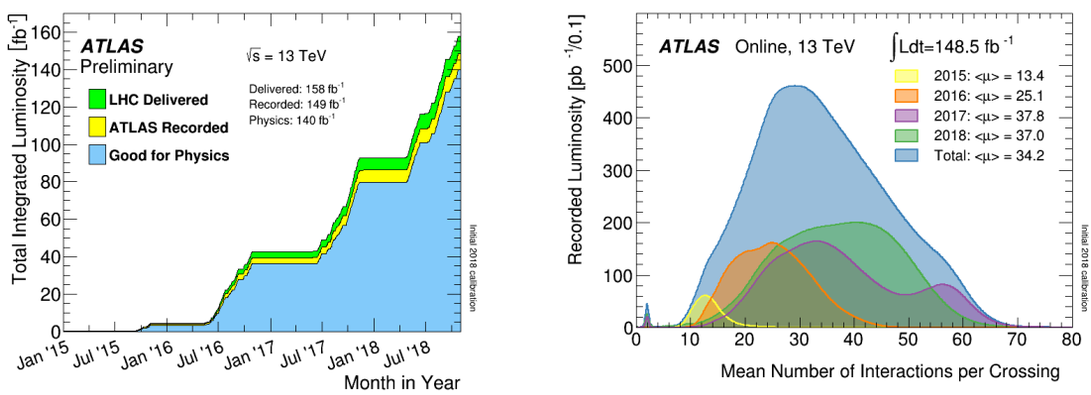

Figure 1.4: ATLAS Run 2 operations: total integrated luminosity of proton-proton collisions (left) and mean number of proton-proton interactions per crossing (right).

Rather than focusing on a particular physics process, the ATLAS detector can measure an entire range of signals, in order to study many phenomena. A field of research of primary interest for the ATLAS experiment is that of Higgs boson measurements, together with the precision Standard Model measurements. Highlights of both research fields are presented in Sections 1.4.1 and 1.4.2, respectively.

After partecipating to the discovery, the ATLAS community is focusing on the precise measurement of the Higgs boson properties. Among the Higgs boson highlight measurements, there is the observation of its $b\bar{b}$ decay channel. This result has been possible only thanks to the dedicated efforts in the jet flavour tagging expertise, necessary to identify the jets originated from b quarks. Another physics sector where the flavour tagging has a crucial impact is the top physics, due to the exclusive branching ratio of the top: $t \to Wb$. Within this field, the Higgs boson associated production with top quark pairs has been one of the highlights of the ATLAS physics program in Run 2.

Another aspect of particular importance in the ATLAS physics program is the determination of Standard Model constants through precision measurements. Dedicated efforts are recently focused in particular on the W boson mass, but more in general to W and Z boson production cross sections. Results from cross section measurements are compared to the most up-to-date theory predictions in order to shed light on the proton content in terms of PDFs. W+jets and Z+jets produc-

tion final states represent major backgrounds for many Standard Model and beyond Standard Model processes. An experimental determination of their cross sections and properties is crucial as well for a correct background estimation.

1.4.1 Higgs boson and top measurements

Higgs boson searches have been carried at LEP [11] and at Tevatron [12], but they did not manage to discover the new particle. LEP contributed to exclude the mass region lower than 114.4 GeV, while Tevatron excluded the 147-180 GeV region. Finally, in 2012 the ATLAS [13] and CMS [14] collaborations discovered a neutral boson compatible with the Higgs boson, with a mass value of ≈ 126 GeV. Further studies reached a better precision on the Higgs mass measurement: the current best estimation of the mass value is 125.18 ± 0.16 GeV [15], combining ATLAS and CMS measurements. With this mass value, it is possible to calculate precisely its production cross sections, the decay rates, the branching ratios and the higgs-fermions couplings.

Feynman diagrams of the main production mechanisms are shown in Figure 1.5. The two Higgs boson production mechanisms having the largest cross section are the gluon gluon Fusion (ggF) and the Vector Boson Fusion (VBF). Other important production mechanisms, due to their clean experimental signature, are the production in association with a vector boson (VH) and with a top pair (ttH).

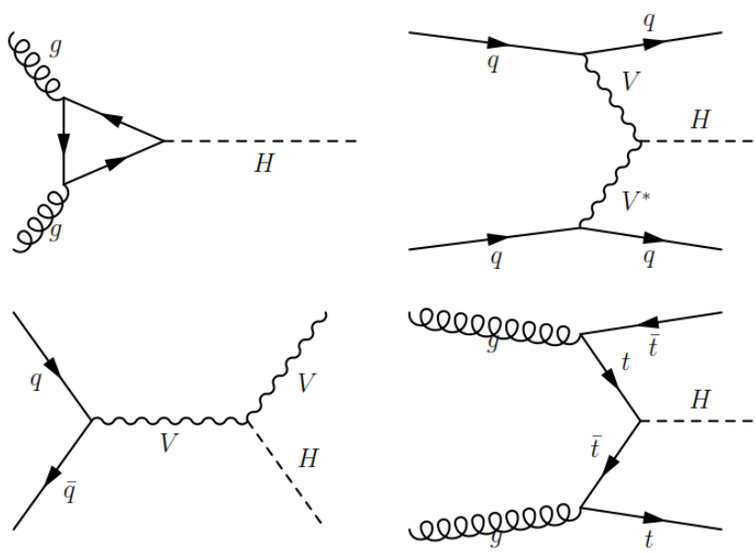

Figure 1.5: Most important Higgs production mechanisms, from top left: gluon-gluon Fusion (ggF), Vector Boson Fusion (VBF), production in association with a vector boson (VH) or with a top pair (ttH).

To study the properties and the couplings of the Higgs boson, it is important to know not only the production rates but also the decay rates (see Figures 1.6 and 1.7). The Higgs boson can decay directly into all possible massive particles, and into pho-

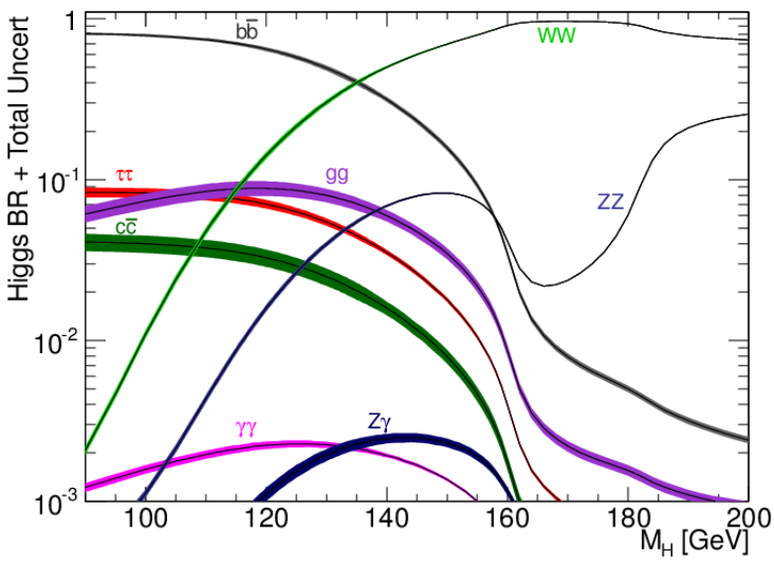

Figure 1.6: Higgs boson decay branching ratios for different mass value: at ≈ 125 GeV the $H \to b\bar{b}$ is the main channel with about 58%, followed by WW (roughly 20%).

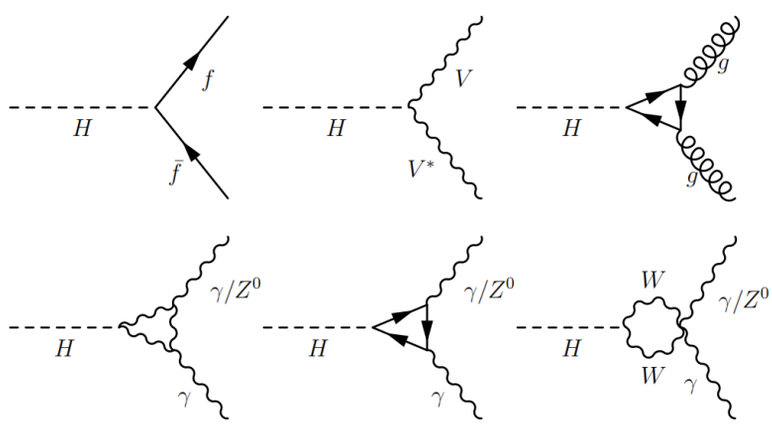

Figure 1.7: Most important Higgs decays channels, from top left: into a fermion pair, a weak vector boson pair, a gluon pair through coupling with a fermion triplet, a $\gamma\gamma$ or a γZ^0 pair through triplets or loop diagrams.

tons and gluons through loop diagrams. With a 125 GeV mass, the main branching ratio is $H \to b\bar{b}$ (58%) followed by $H \to WW$ (roughly 20%), with decreasing branching ratio but not minor importance: gg, $\tau\tau$, ZZ, $c\bar{c}$, $\gamma\gamma$, $Z\gamma$.

The Higgs discovery made by the ATLAS and CMS collaborations was performed studying the ZZ and $\gamma\gamma$ decay channels, because these signatures are clearly identified in the detector. On the opposite, at a hadron collider, there is plenty of quark production and this represents a large background for the search in the $H \to b\bar{b}$ channel. Also for this decay channel, data indicate that the newly discovered particle is compatible with what expected for the SM Higgs boson. In order to measure the Higgs properties, it is essential to measure all the Higgs couplings, included the one with b-quarks.

The b-tagging plays a crucial important role in those searches, expecially in the $H \to b\bar{b}$ channel: this channel has been studied extensively at ATLAS with Run 1 and Run 2 data, with increased energy and luminosity (7 TeV, 8 TeV and 13 TeV results are shown in Figure 1.8). This huge effort led to the evidence of $H \to b\bar{b}$ [16], announced by the ATLAS collaboration in July 2017, and then to the observation [17], announced in August 2018.

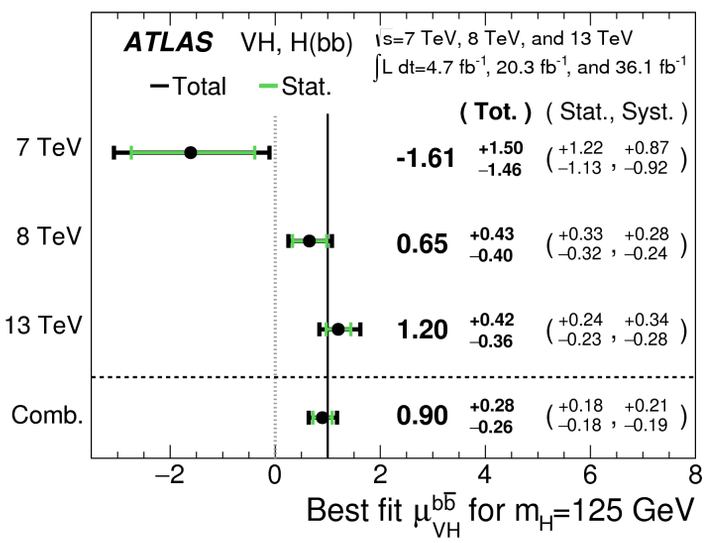

Figure 1.8: Results of the Higgs measurements in the $H \to b\bar{b}$ channel performed by the ATLAS experiment with 7, 8 and 13 TeV data.

The largest source of Higgs bosons is the production via gluon fusion, but the $gg \to H \to b\bar{b}$ channel is not experimentally measurable because of the high background of $b\bar{b}$ events (10^7 more frequent than the signal). The experimental accessible measurements are instead those performed in the more clean associated production of a Higgs with a W or Z vector boson ($VH \to b\bar{b}$), that allows a easier background rejection, selecting leptons coming from Vector bosons decay. The distribution of the invariant mass of the b-jet pair is presented in Figure 1.9 in data after subtraction of all backgrounds, except for the WZ and ZZ diboson processes.

Top quark is the heaviest particle ever discovered with a measured mass of 173.0 ± 0.4 GeV [15]. It was discovered at Tevatron [18, 19] in 1995, and since then many measurements have been carried out in order to determine its properties. Top quark lifetime is so low ($\sim 10^{-25} s$) that it is the only quark decaying before the hadronization process occurs. For this reason, no hadrons containing top quark can be observed. The top quark decays almost exclusively into a bottom quark and a W boson via an electro-weak process ($t \to Wb$ branching ratio being around 99% [15]): the correct identification of a b-jet allows to study in deep the top quark and its properties. The precise measurement of top quark production cross sections and decay channels is important because events having top quarks in the final state

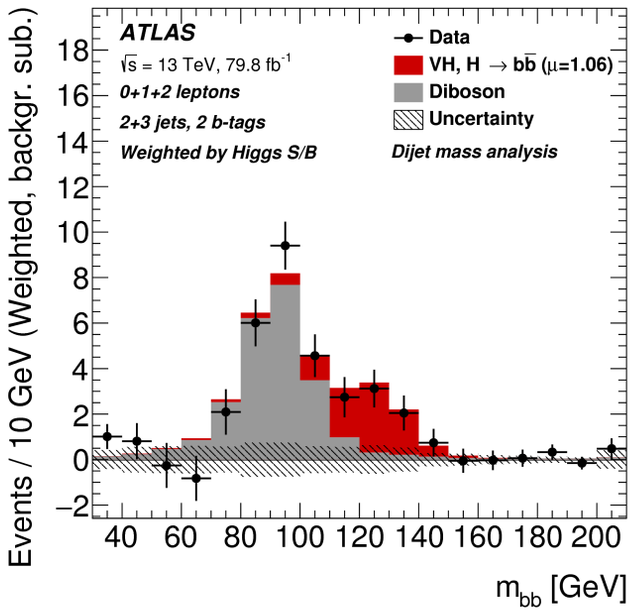

Figure 1.9: Distribution of the invariant mass of the b-jet pair, measured by ATLAS in the $VH \to b\bar{b}$ channel, after subtraction of all backgrounds, except dibosons.

are one of the dominant backgrounds in many physics analyses searching for new physics beyond Standard Model.

One of the most intriguing measurement in the Higgs sector is the search for Higgs boson associated production with a top pair (ttH). It is one of the most complicated Higgs measurements as well, since the production rate of ttH is very low (about 1% branching ratio) and its final state involves a high number of objects among top and Higgs decay products. There is great interest in this measurement because the top quark has a very large mass; therefore, the strength of its coupling with the Higgs boson is high, higher than any other coupling. The direct measurement of the Higgs-to-top coupling is important to confirm the indirect results, that can be derived starting from other Higgs boson couplings measurements.

The ATLAS collaboration announced to have found statistically significant evidence of the ttH production [20] in 2017 (see Figure 1.10), then the observation was announced in 2018 [22] (see Figure 1.11). Among the studied decay channels, there is also $ttH \to b\bar{b}$ [21], which involves 4 b-jets in the final states. Due to its complexity, it was categorized into 19 regions as a function of the number of jets and b-jets, and the quality of the b-jet identification.

1.4.2 SM precision measurements

Among recent highlights in ATLAS physics results, there is the precise measurement of the mass of the W boson [23], a parameter closely related to the masses of the top quark and the Higgs boson. Measuring the W mass is a Standard

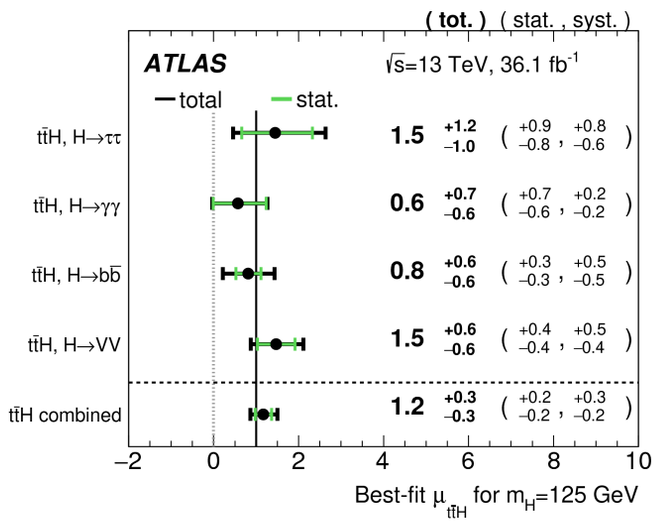

Figure 1.10: Results of the ATLAS measurement of the Higgs boson associated production with top quark pairs, in different Higgs boson decay channel, performed on 13 TeV data.

Model test itself, but also a possible way to look for physics beyond the Standard Model, since any deviation from the theory prediction would be a sign of new physics. The W mass was measured previously at LEP and Tevatron, yielding a world average of 80.385±0.015 GeV, which is consistent with the SM constraints of 80.358 ± 0.008 GeV. The ATLAS collaboration has recently reported the first measurement of the W mass at the LHC [23], based on 4.6 fb^{-1} 7 TeV data, after years of accurate calibrations. The value measured by ATLAS, 80.370 ± 0.019 GeV, matches the precision of the Tevatron CDF experiment and is consistent with both the SM prediction and combined measurements (see Figure 1.12). The value measured by ATLAS is compared to results from the LEP (ALEPH, DELPHI, L3 and OPAL) and the Tevatron experiments (CDF and D0). Measured values of mass for positively and negatively charged W bosons are also shown.

Significant contributions to W production from second-generation quarks (strange and charm) are expected at LHC, compared to LEP and Tevatron: the enhanced amount of W boson produced due to heavy quarks and the ratio of valence and sea quarks in the proton affect the W boson transverse-momentum distribution and its polarisation, which makes the measurement sensitive to the proton PDFs.

Another recent ATLAS result, even more sensitive to proton PDFs, is the $W \to l\nu$/Z$\to ll$ cross section ratio measurement, where W and Z boson production cross sections measured at 7 TeV [24] with high precision are combined into a ratio, allowing to reduce some of the common systematics. The experimental precision reached is comparable and sometimes better than the one on the theoretical predictions. In Figure 1.13, the ATLAS result is compared with predictions obtained adopting different PDFs: in all cases, the predicted cross section ratio values are higher than those measured in data, clearly pointing out the need for improvements in the description of the proton structure.

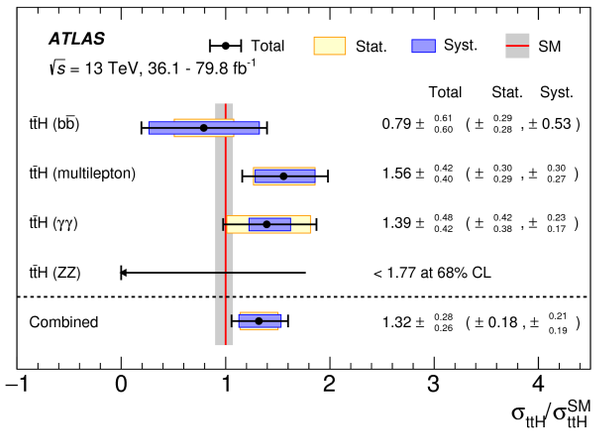

Figure 1.11: Combined ttH production cross section, as well as cross sections measured in the individual analyses (79.8 fb^{-1}: $\gamma\gamma$, ZZ; 36.1 fb^{-1}: multilepton, $b\bar{b}$), divided by the SM prediction. The black lines show the total uncertainties and the bands indicate the statistical and systematic uncertainties. The red vertical line indicates the SM cross-section prediction and the grey band represents the PDF uncertainties and the uncertainties due to missing higher-order corrections.

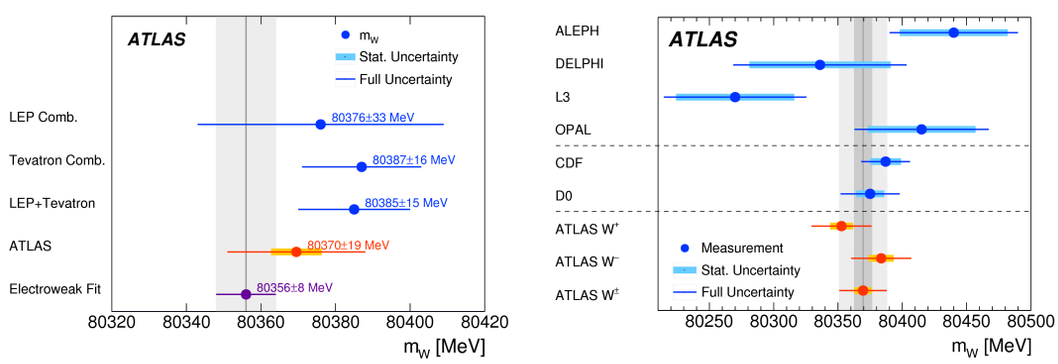

Figure 1.12: W boson mass measured by ATLAS compared with predictions and results from other experiments.

A broad interest in the LHC community is growing towards the strange quark PDF: several measurements are aiming at constraing further and further its values, currently affected by high uncertainties. Cross section measurements both of inclusive W/Z production and of specific W/Z+jets processes (for example $W+c$ production) provide constraints on the proton PDFs. The strange quark PDF is of particular interest due to a tension between experimental results and the predictions [25]. The previous ATLAS W and Z boson cross section measurements and its QCD interpretation suggested that the light quark sea is flavour symmetric. The ratio of the strange-to-anti-down quark densities, r_s, was found to be close to unity within 20% uncertainty, where r_s is calculated as:

$$r_s = \frac{0.5(s + \bar{s})}{\bar{d}}. \tag{1.5}$$

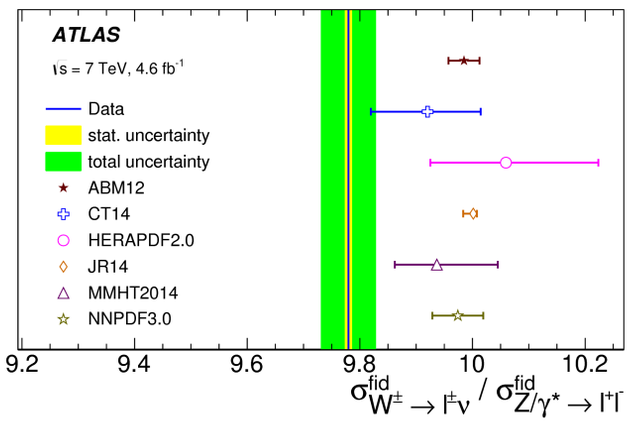

Figure 1.13: Fiducial cross sections times leptonic branching ratios of the $W \to l\nu$/Z$\to ll$ ratio. The data (solid blue line) are shown with the statistical (yellow band) and the total uncertainties (green band). The uncertainties of the theoretical calculations correspond to the PDF uncertainties only.

The recent ATLAS high precision measurement with 7 TeV data has been used to derive a new version of the ATLAS based PDF set, *ATLAS-epWZ16*, that supersedes the previous *ATLAS-epWZ12* set. In the new set, the ratio of strange-to-light sea-quark densities in the proton is determined more accurately and is established to be close to unity in the sensitivity range of the data, suggesting unsuppressed strangeness as a function of x. In particular, the strange-to-light sea-quark ratio, R_s, built as:

$$R_s = \frac{s + \bar{s}}{\bar{u} + \bar{d}}, \tag{1.6}$$

is found to be higher than unity in the x range considered ($10^{-3} < x < 10^{-1}$), with larger model uncertainties in the high and low x regions (see Figure 1.14). The ATLAS data have the best sensitivity in the region with $Q^2 = 1.9$ GeV^2 and $x = 0.023$, where the R_s is measured to be 1.13 ± 0.05 (exp) $\pm$ 0.02 (mod) $^{+0.01}_{-0.06}$ (par). With this high precision measurement, ATLAS is definitely accessing the proton structure. Theoretical predictions, based on calculations accurate to Next-to-Next-to-Leading Order (NNLO) for QCD and to Next-to-Leading Order (NLO) for electroweak processes based on different PDF sets, are compared to the ATLAS result.

Moreover, both the ATLAS [26] and CMS [27] experiments have measured the W+c process cross section, using $\sqrt{s} = 7$ TeV pp collision data collected at the LHC in 2011. The ATLAS result [26] suggested that the ratio of strange-to-down sea-quark distributions r_s is compatible with the unity for a wide range of x (Figure 1.15, left). Recently, an updated measurement performed by the CMS experiment [28], with $\sqrt{s} = 13$ TeV pp collision data collected at the LHC in 2016, has shown that r_s decrease with the increase of x (Figure 1.15, right).

In this context, the preparatory studies for the measurement of the W+c cross section with Run 2 ATLAS data are presented in this thesis (see Chapter 11).

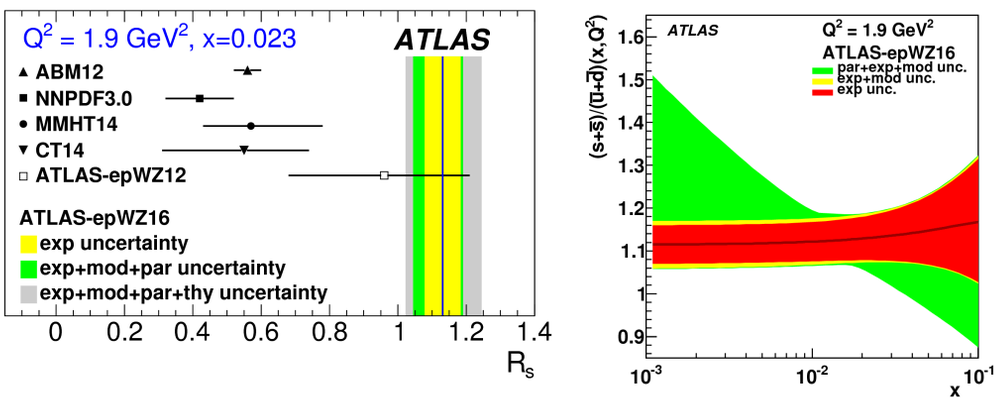

Figure 1.14: Left: R_s ratio of the *ATLAS-epWZ16* PDFs shown in the region of maximum sensitivity of the ATLAS data, $10^{-3} < x < 10^{-1}$. Red, yellow and green bands represent the experimental (exp), model (mod) and parameterization (par) uncertainties, respectively. Right: R_s in the region of ATLAS best sensitivity, Q^2 = 1.9 GeV^2 and x = 0.023. Bands present result and its uncertainties from experimental data, QCD fit, and theoretical uncertainties.

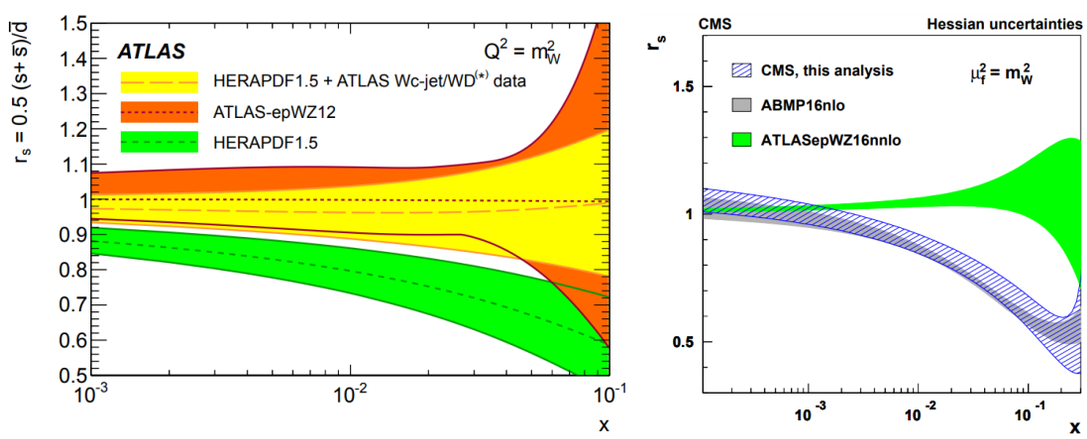

Figure 1.15: Ratio of strange-to-down sea-quark distributions r_s as a function of x at $Q^2 = m_W^2$. Left: HERAPDF1.5 PDF compared to the fit including ATLAS W+c-jet/W+D* data, and *ATLAS-epWZ12*. Right: ABMP16 PDF compared to the fit including CMS W+D* data, and *ATLAS-epWZ16*.

Chapter 2

The ATLAS detector

The ATLAS detector is 46 m long with a 25 m diameter and its overall weight is over 7000 tons (see Figure 2.1). The ATLAS coordinates are reported in Section 2.1. ATLAS is composed by three different sub-detectors: the Inner detector (Section 2.2), the Calorimeters (Section 2.3) and the Muon spectrometer (Section 2.4). These components cover the interacting point, embracing it in the shape of a cilinder: each of the three sub-detectors is divided into a barrel section (around the collision point, in the central region) and two end-caps (at the two sides, in the forward region). In particular, the Inner detector measures charged particles momentum and provides their reconstructed trajectories; the Calorimeters measure the energy of hadrons, electrons, positrons and photons; the Muon spectrometer identifies muons and measures their momentum. To measure properly the particles momentum and their charge sign, ATLAS is equipped with a Magnet system (Section 2.5) composed by a superconducting solenoid (around the Inner detector) and 8 large superconducting toroids (around the Calorimeters). Proton-proton interactions occur at a very high rate: the data acquisition infrastructure (Section 2.6) manages the huge data flow through a dedicated trigger system which selects the most interesting physics events. In the next years the ATLAS detector will undergo several upgrades, including the complete replacement of its tracking system: an introduction to the silicon tracking detectors is presented in Chapter 3, with a focus on the Pixel detectors technology and the future tracker: the Inner Tracker (ITk).

2.1 ATLAS coordinates

The ATLAS coordinate system has the origin in the nominal collision point, with the Y axis pointing vertically upwards, the X axis pointing towards the center of LHC ring and the Z axis pointing towards the direction of the counter-clockwise circulating beam. Actually, the Y axis points upwards with a 0.704° tilt, because of the LHC plane inclination (see Figure 2.2).

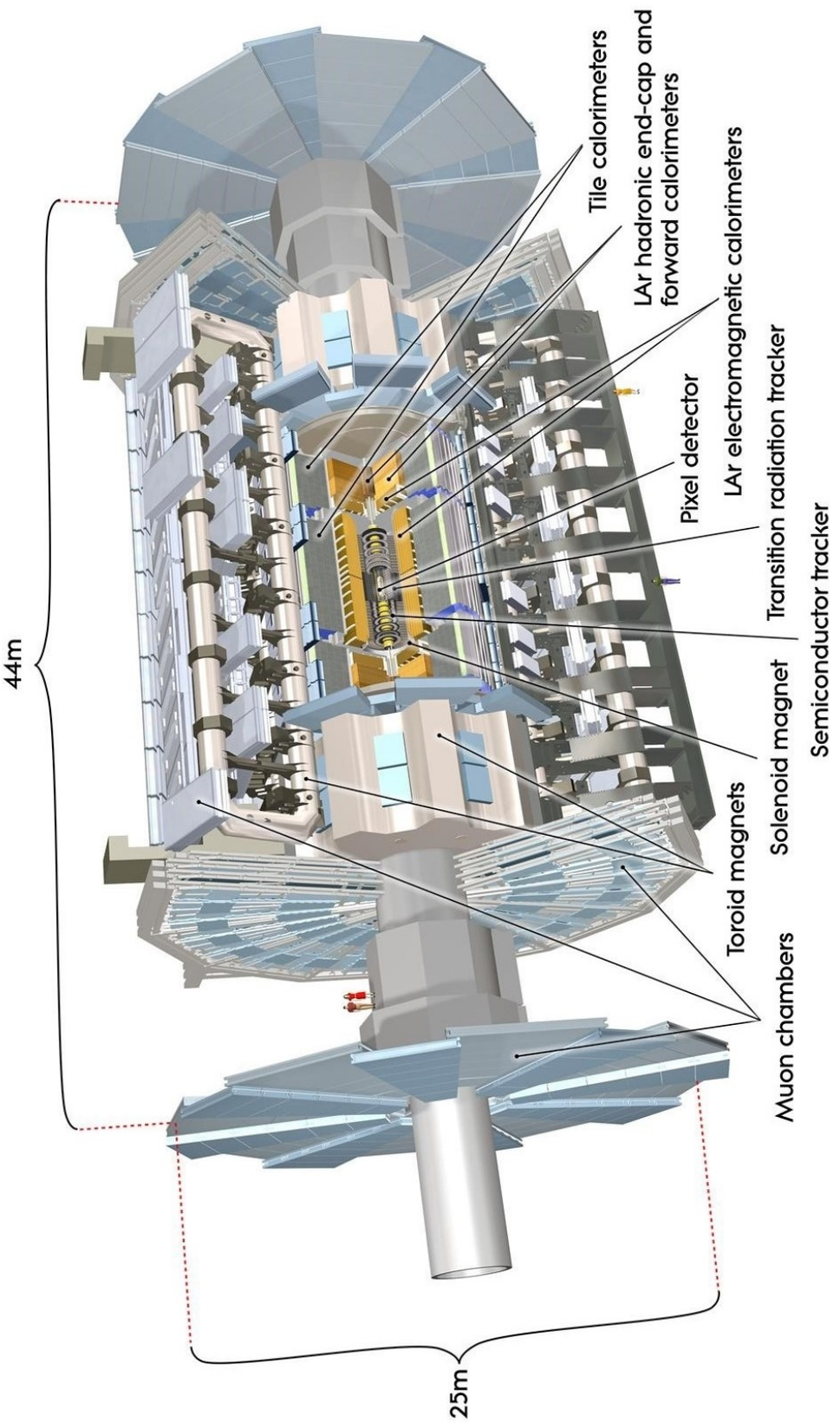

Figure 2.1: Full view image of the ATLAS detector. [29]

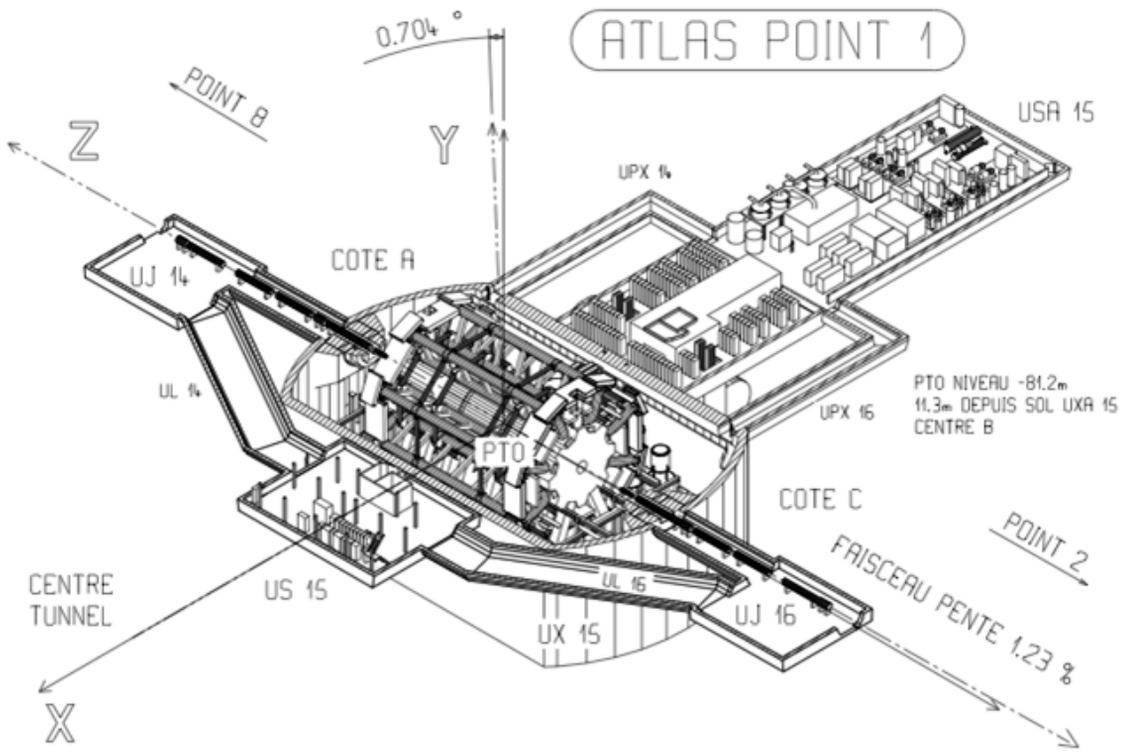

Figure 2.2: Interaction Point 1: ATLAS cavern and coordinate system.

Instead of carthesian coordinates, a system of cylindrical coordinates is preferred:

$$(x, y, z) \rightarrow (r, \phi, \theta). \tag{2.1}$$

The three cylindrical coordinates are: the radial coordinate r, the azimuthal angle ϕ, lying in the transverse plane with respect to the beam, and the polar angle θ, defined as the angle between the particle three-momentum $\mathbf{p}$ and the positive direction of the beam axis. The polar angle coordinate is often expressed in terms of the pseudorapidity η (widely used in high energy physics), where η is defined as a function of the polar angle θ:

$$\eta \ = \ -\ln(\tan\frac{\theta}{2}). \tag{2.2}$$

Many analyses often require a selection on a precise pseudorapidity range ($|\eta| < 2.5$) corresponding approximately to the interval between $\theta = 9.39°$ and $\theta =$ -9.39°, since in this region there is a better instrumental coverage.

Starting from the cylindrical coordinates, all vectors, including cynematic vectors, are expressed in these terms (p_T, η, ϕ), where the transverse momentum p_T is defined as the component of the three-momentum $\mathbf{p}$ perpendicular to the beam axis:

$$p_T \ = \sqrt{{p_x}^2 \ + \ {p_y}^2}. \tag{2.3}$$

2.2 Inner detector

The Inner Detector (ID) [30] is the closest to the the interaction point, surrounding the beampipe. It is composed by 4 subdetectors (see Figure 2.3), from the inner to the outer most: the Insertable B-Layer (IBL), the Pixel detector, the Semi Conductor Tracker (SCT) and the Transition Radiation Tracker (TRT). The silicon detectors (IBL, Pixel and SCT) are arranged in cylindrical layers: the barrel layers, made by longitudinal bars covering the interaction region, and the end-cap disks, at the two sides of the barrel. In a similar way, the straw tubes of the TRT are distributed longitudinally in the barrel and radially in the disks. Each layer of the subdetectors provides a 1D coordinate (hit) of the particle transit. Subsequently the hits are connected, reconstructing a 3D track. Immersed into a 2 T magnetic field generated by the solenoid, the ID provides precise charged particle identification, their trajectories and vertex reconstruction. Basic characteristics of the subdetectors are resumed in Table 2.1, more details are provided in the following Sections.

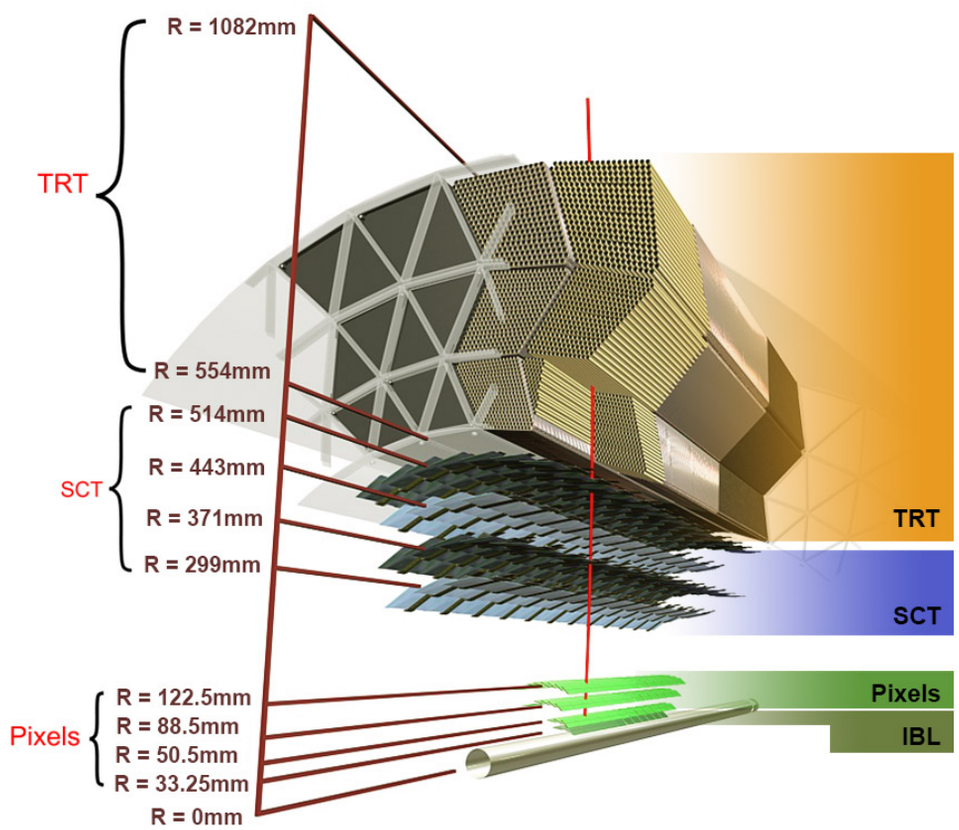

Figure 2.3: Overview of the barrel section of the Inner Detector after the IBL insertion (2015). [29]

Subdetector	Element size	Intrinsic resolution [μm]	Barrel layers radius [mm]
IBL	50 μm $\times$ 250 μm	8 (R - ϕ) $\times$ 40 (z)	33.2
Pixel	50 μm $\times$ 400 μm	10 (R - ϕ) $\times$ 115 (z)	50.5, 88.5, 122.5
SCT	80 μm	17 (R - ϕ)	299, 371, 443, 514
TRT	4 mm	130 (R - ϕ)	from 554 to 1082

Table 2.1: Basic characteristics of the ID subdetectors: element size, intrinsic resolution and barrel layer radius. For SCT and TRT the element sizes refer to the spacing of the readout strips and the diameter of the straw tubes, respectively.

Insertable B-Layer

The Insertable B-Layer (IBL) [31] has been introduced between the innermost Pixel layer (the B-layer) and the vacuum chamber containing the beams (beampipe) during the first Long Shutdown occurred between Run 1 and Run 2. A new Beryllium beampipe was built (reducing the radius from 29 mm to 25 mm) in order to obtain enough space for the IBL installation. IBL is composed by 14 staves each supporting 20 modules, mounted longitudinally on the beampipe (see Figure 2.4), at about 33 mm from the interaction point. In particular, each stave is equipped with 12 Planar sensors (in the central region of the stave) and 8 3D sensors (in the forward region of the stave, 4 for each side). The Planar sensors are bump-bonded to two Front-End readout chips, while the 3D sensors are connected to a single Front-End chip. In particular, Planar sensors are silicon double chip sensors ($n^+ - in - n$) while 3D sensors are single chip sensors ($n - in - p$).

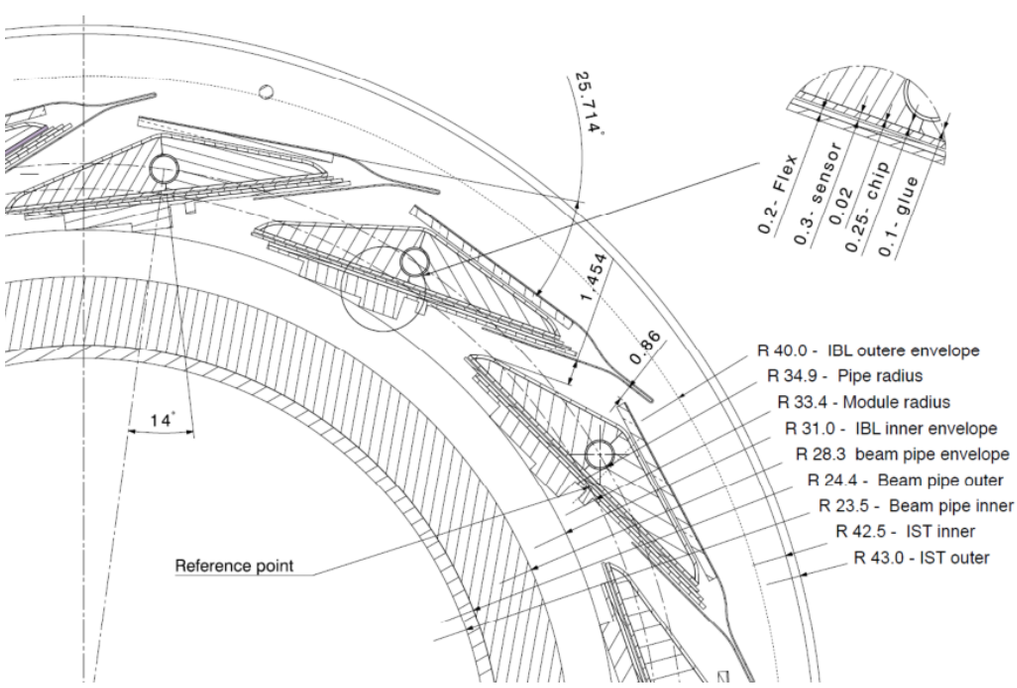

Figure 2.4: Radial view of IBL layout: the staves are mounted between the beampipe and the IBL Support Tube (IST).

Given the fact that semi conductor detectors are quite sensitive to radiation, the main purpose of the IBL is to provide a new additional layer, less sensitive to radiation damage, increasing the robustness of the track reconstruction of the detector. Furthermore, the addition of an extra layer placed closer to the interaction point considerably improves the vertex reconstruction capability of the detector.

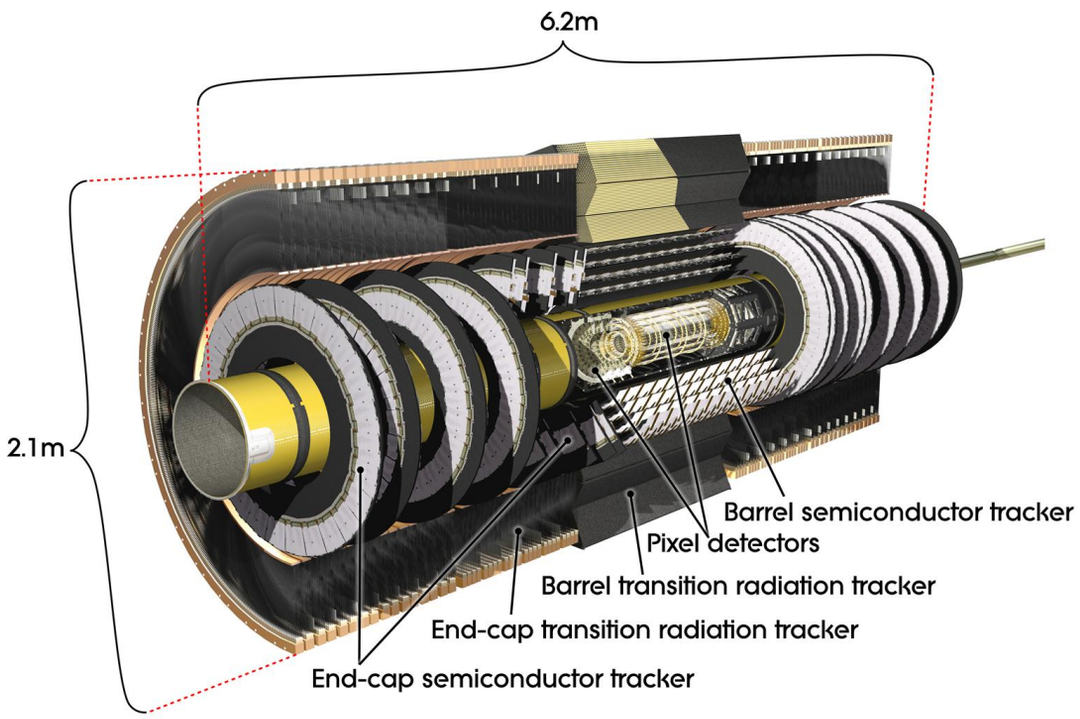

Figure 2.5: Overview of the Inner Detector before introducing IBL: Pixel detector, Semi Conductor Tracker and Transition Radiation Tracker.

Pixel detector

The Pixel detector [32] is located around the interaction point, sorrounding IBL. It is composed by three concentric barrel layers (mean radius: 5.05 cm, 8.85 cm and 12.25 cm; length: 80.1 cm) and two end-caps of three disks each (mean radius: 17 cm; distance from the interaction point: 49.5 cm, 58 cm and 65 cm): this allows to provide three hits for a precise track reconstruction. Thanks to Pixel detector it is possible to identify collision vertices and to measure the impact parameters of tracks with high resolution (impact parameters define the distance of closest approach between the track and the primary interaction vertex position, see Section 7.1). With approximately 80 million silicon sensors[1], the Pixel detector covers a pseudorapidity range of $|\eta| < 2.5$ with an extremely high granularity. It reaches an accuracy of 10

[1]The Pixel detector channels, together with the IBL channels, reach a total of about 100 million channels, each of them individually calibrated.

μm in R - ϕ and 115 μm in z in the barrel, 10 μm in R - ϕ and 115 in R in the disks. Its role is crucial to perform b-tagging as its high spatial resolution allows to measure with high precision the distance between tracks and the primary interaction vertex.

Semi Conductor Tracker (SCT)

The Semi Conductor Tracker (SCT) [33,34] consists of 4088 modules of silicon strips arranged in four concentric barrels and two end-caps of nine disks each, for a total surface of 63 m^2. The barrel region uses two different micro-strips with one set of strips in each layer parallel to the beam direction and a relative angle of 40 mrad. The end-cap region has a set of strips running radially and a set of stereo strips at an angle of 40 mrad. The SCT is designed to provide a minimum of four three-dimensional position measurements per track: it allows precise measurements of track momenta, vertex position and impact parameter with an accuracy of 17 μm in R - ϕ and 580 μm in z.

Transition Radiation Tracker

The Transition Radiation Tracker (TRT) [35] is both a straw drift-tube tracker and a transition radiation detector. It is divided in two barrel sections and two end-caps. The detector consists of about 300000 proportional drift tubes (straws) with 2 mm diameter; each tube is filled with a gas mixture of Xe, CO_2 and O_2, with 5-10 mbar over-pressure. The barrel sections are composed by 144 cm long straws disposed parallel to the beam direction; the end-caps are composed by radially disposed 37 cm long straws. The accuracy is not high (about 130 μm per straw in R - ϕ), anyway the high number of hits ($\sim$ 36 per crossing track) compensates the low precision, providing an accurate momentum measurement.

2.3 Calorimeter

The Calorimeter system [36] sorrounds the ID and the 2T solenoid (see Figure 2.6): it is composed by an electromagnetic calorimeter designed to measure the energy and provide identification of electrons/positrons and photons and by an hadronic calorimeter for energy measurement of charged and neutral hadrons. With an overall radius of 4.23 m and a length of 13.3 m, with the hadronic calorimeter sorrounding the electromagnetic one, it covers a total range in pseudorapidity $|\eta| < 4.9$. It is consists in a barrel section and two end-caps for both electromagnetic and hadronic calorimeter, plus a forward calorimeter in the forward region (the region at small angle with respect to the beam axis). Dedicated sections of the calorimeter have trigger capabilities, exploited for the fast event selection.

In particular the Calorimeter system can measure with high precision the energy, position and shower shape of electrons/positrons, photons and jets. With these

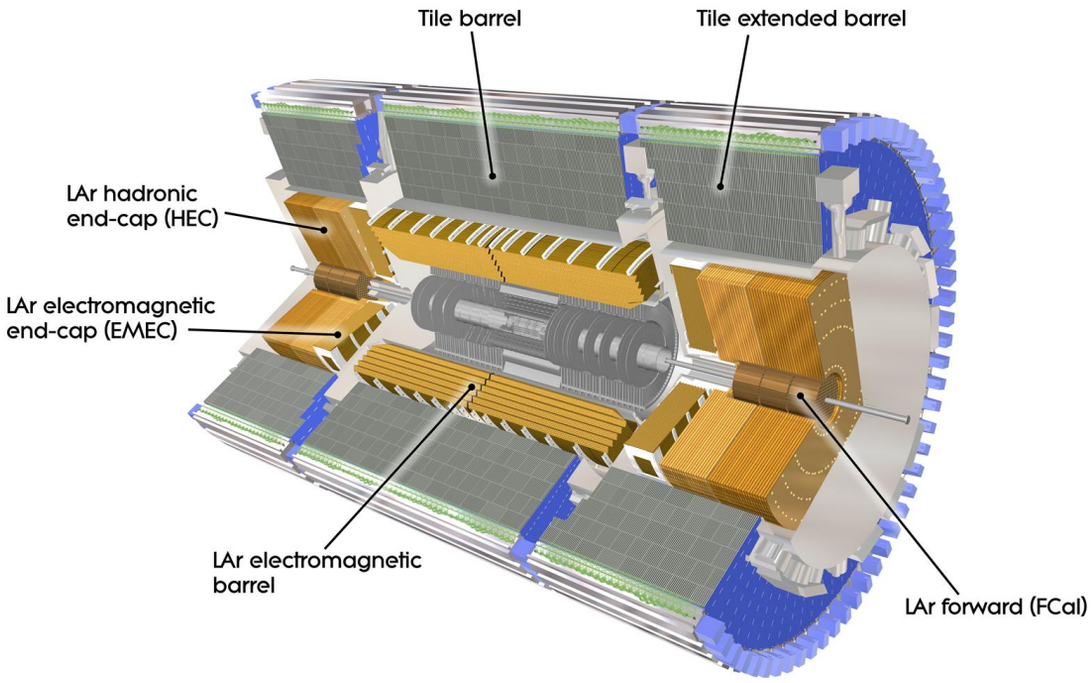

Figure 2.6: The ATLAS Calorimeters system: electromagnetic, hadronic and forward sections. [29]

measurements, it contributes to the definition of missing transverse momentum and to particle identification. It is capable of disentangling electron/positron and photon showers from showers coming from hadrons and tau decays and QCD background up to the TeV energy scale.

Electromagnetic Calorimeter

The electromagnetic calorimeter uses Lead layers as absorber material to generate the particle shower and liquid Argon layers as active material to measure energy and position. It is composed by a barrel section ($|\eta| < 1.475$, more than 26 radiation lengths) and two end-caps ($1.375 < |\eta| < 3.2$, more than 24 radiation lengths). The barrel section is divided in two identical half-barrels, while each endcap is divided into two coaxial wheels. This geometry enhances the η precision measurements and the γ/π_0 and the e/π separation.

Hadronic Calorimeter

The hadronic calorimeter uses different materials for barrel and end-caps: the barrel section uses Iron as absorber material and scintillating tiles as active material, while the end-caps use Argon technology with Copper as absorber material. The barrel section is composed by the central tile barrel ($|\eta| < 1.0$) and by two lateral

tile extended barrel ($0.8 < |\eta| < 1.7$). The hadronic calorimeter end-caps cover a pseudorapidity range $1.5 < |\eta| < 3.2$. This approach contains the hadrons from propagating further in the muon system and provides good measurements of missing transverse momentum.

Forward Calorimeter

The forward calorimeter uses copper and tungsten as absorber materials and liquid argon as active material, covering the forward region between $3.2 < |\eta| < 4.9$, a region with very high level of radiation. It is composed by one electromagnetic and two hadronic calorimeter layers for each side of the interaction point, longitudinally 1.2 m far from the Inner detector.

2.4 Muon spectrometer

The Muon spectrometer [37] is the outermost of the ATLAS sub-detectors (see Figure 2.7). Thanks to the magnetic field produced by the air-core toroid system (described in Section 2.5), it measures the kynematic properties of the muons, through the deflection of their tracks. It is designed to detect charged particles in the pseudorapidity range $|\eta| < 2.7$, measuring the momentum with small uncertainty; it has also trigger capability in the pseudorapidity range $|\eta| < 2.4$. In order to enhance the momentum resolution, the tracks recostructed in the muon spectrometer can be extrapolated back to the internal region of the ATLAS detector, matching the Inner detector track with the track provided by the Muon spectrometer. The muon system is divided in barrel and end-cap regions, employing four different detector technologies: Monitored Drift Tube chambers (MDT), Cathode Strip Chambers (CSC), Resistive Plate Chambers (RPC) and Thin Gap Chambers (TGC). In particular the MDT and the CSC measure with high accuracy the 2D spatial coordinates of the track: they are the tracking core of the muon system because of their high spatial resolution (80 μm). The RPC and the TGC are the trigger core of the muon system: they provide a faster but less precise signal, useful for trigger decision.

2.5 Magnet system

The magnet system is made of two different solutions: a central superconducting solenoid and 3 air-core superconducting toroids. The solenoid surrounds the Inner detector and provides a 2 T axial magnetic field that bends particles trajectories. It is 5.3 m long, with a mean radius of 1.25 m; it is cooled at 4.5 K by liquid helium. The toroidal field is generated by 3 huge air-core toroids: one in barrel region and two in the end-cap regions[2]. Each air-core toroid consists of 8 coils mounted symmetrically

[2]The magnetic field intensity (1 T for the barrel and 0.5 T for the end-cap regions) are indicative, since the field is not uniform across the whole area.

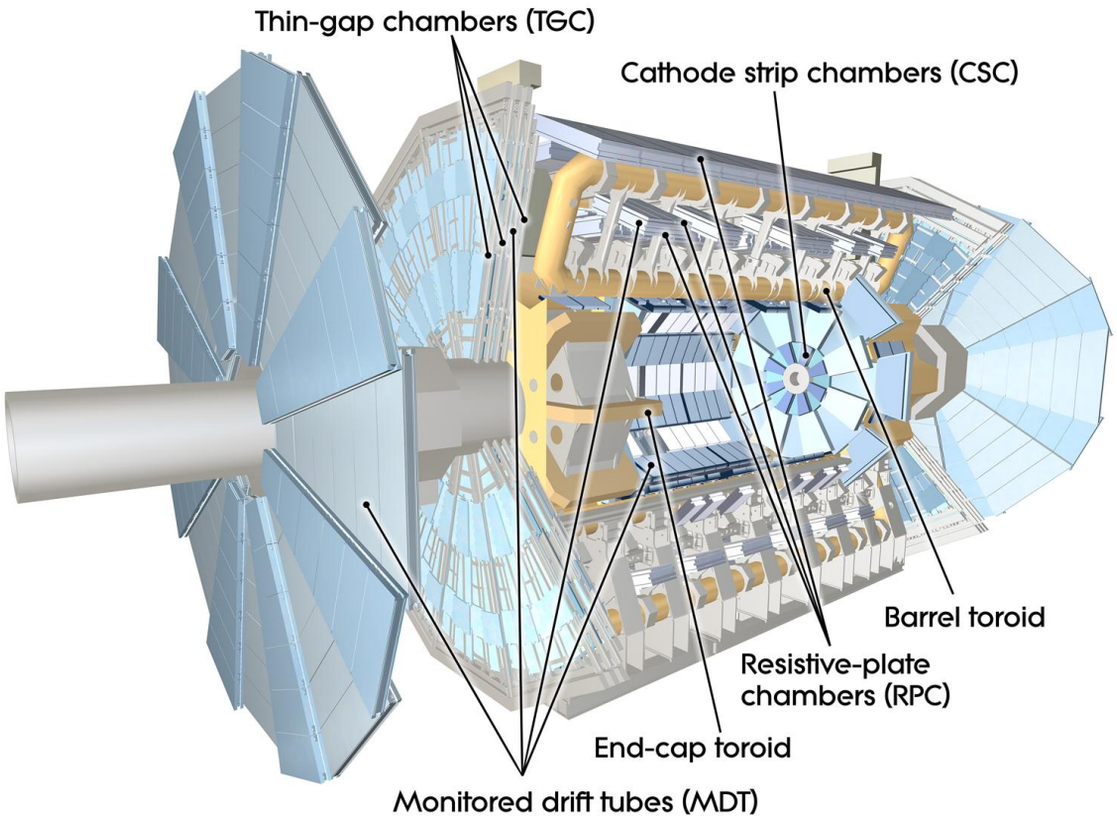

Figure 2.7: Overview of the Muon spectrometer. [29]

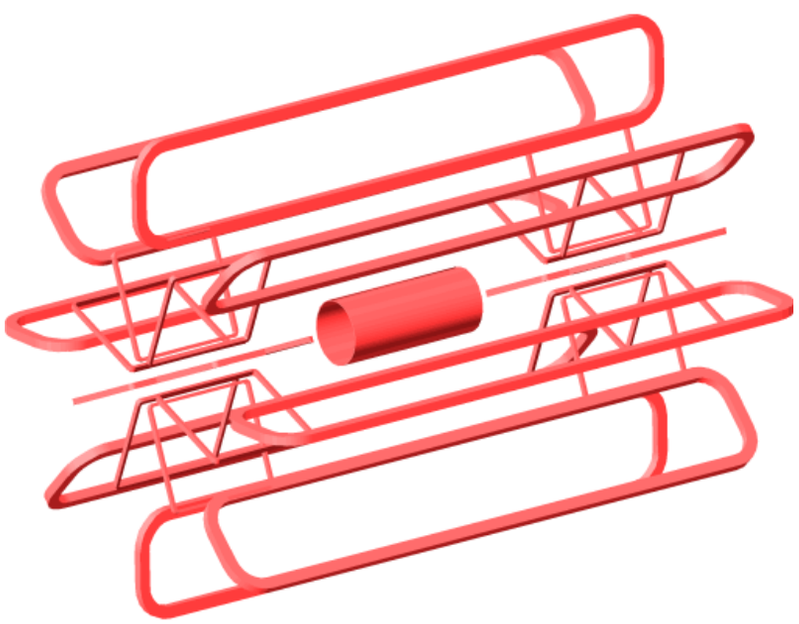

Figure 2.8: The Magnet system: the superconducting solenoid and the toroids.

in ϕ, distanced of 45° around the beam axis. The barrel toroids extend for more than 25 m with an inner diameter of 9.4 m and an outer diameter of 20.1 m. The end-cap toroids have a length of about 5 m, with an inner diameter of 1.6 m and an outer diameter of 10.7 m.

2.6 Trigger and data acquisition

The high event rate produced by LHC collisions is impossible to handle with any available storage technology, while at the same time, the majority of the events are not interesting. The trigger infrastructure performs a drastic selection of the events, reducing the data flow to an acceptable level before transferring it to permanent storage. The data acquisition system (DAQ) reads the data from the detector and manages the data flow until the permanent storage. These two systems are strictly interacting, they are often referred to as a unique system, the TDAQ. A schematic view of the Run 2 ATLAS trigger and DAQ infrastructure is visible in Figure 2.9.

At the design luminosity ($\mathcal{L} = 10^{34}\ cm^{-2}s^{-1}$), LHC collisions produce about 23 interactions per bunch crossing: this means a data production of 4000 Gb/s for a bunch crossing rate of 40 MHz (1 bunch crossing event per 25 ns). The ATLAS trigger system [38] is capable to reduce this huge data quantity selecting the interesting events with physics-oriented criteria. During Run 1 the trigger system was divided in 3 levels: Level-1, Level-2 and Event Filter, while from Run 2 the last two levels are merged to form a unique software based trigger, the High Level Trigger.

The Level 1 trigger selects Regions of Interest (RoI) using the Calorimeters and the Muon spectrometer information, searching above all for high transverse momentum particles, the most interesting particles produced in the collisions. Within 2.5 μs, the hardware processors select the events with a roughly 100 kHz accept rate.

The High Level Trigger uses the complete detector information: fine granularity data coming from the Inner detector, the Calorimeters and the Muon spectrometer. It performs ID track reconstruction and searches among fully-built events within 4 s, reducing the rate to a few hundreds of Hz. Adopting offline-like algorithms, in some cases exactly the ones used for final reconstruction, this step can be performed only at the end of the chain, thanks to the previous data reduction.

During the selection, the trigger levels exchange information in the form of RoI and recostructed events with the data acquisition infrastructure. This information exchange ends with the final permanent data storage of the selected events on the ATLAS software infrastructure.

Since many interactions are produced for each bunch crossing, when saving data for a particular triggered event, also the information coming from all the other bunch crossing interactions is recorded: the events collected in this way are defined pile-up events. The ATLAS experiment developed different solutions to reduce the impact of pile-up contamination on physics analyses (see Section 7.1).

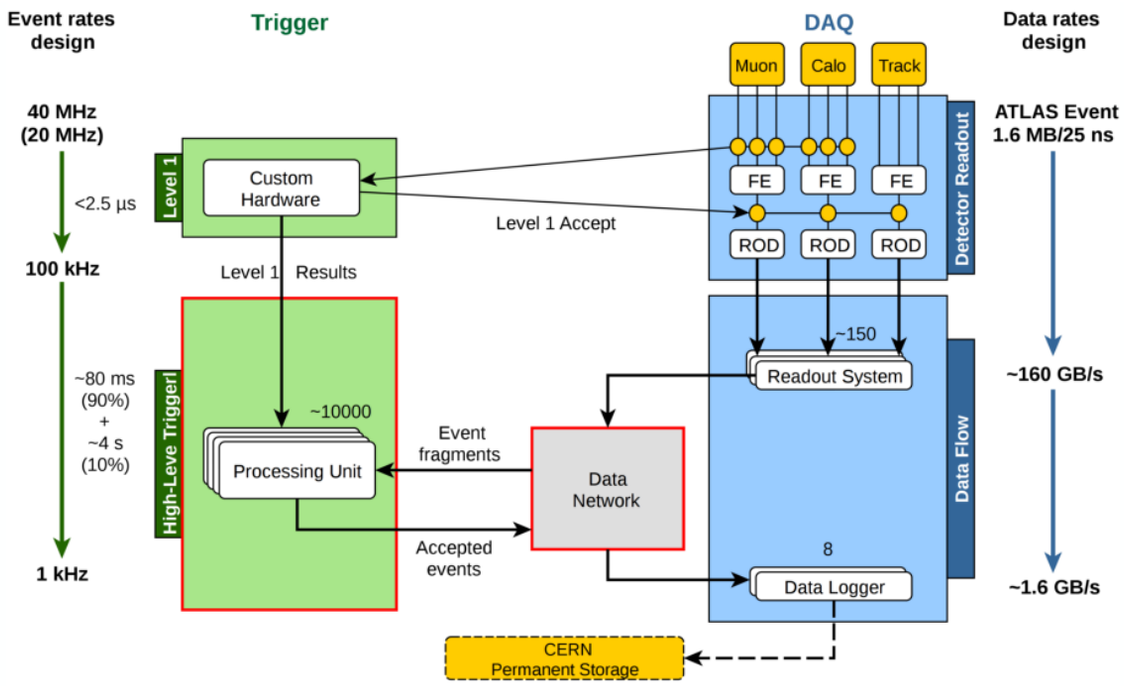

Figure 2.9: Schematic view of the Run 2 ATLAS trigger and DAQ infrastructure.

2.7 Software infrastructure

The ATLAS experiment developed a specific framework for the data analysis, MC simulation and event displaying: the Athena framework [39, 40]. Athena is based on Gaudi architecture [41], previously developed for LHCb experiment, with many specific improvements required for ATLAS data analysis. The framework can generate simulated samples and reconstruct both real and simulated events. To perform these tasks, it is possible to run a chain of algorithms in one job or to split the assignment into several jobs.

ATLAS software has a hierarchical structure: Athena is split in Projects and these ones are organized in Packages, a complete collections of projects is identified by an overall release number (i.e. release 21); sometimes sub-release versions are also identified (i.e. release 20.1, release 20.7). Subsequent releases usually include major improvements and optimizations of the available algorithms, as well as new algorithms and tools.

Event generation and detector simulation

The event generation is performed with specific tools, such as Pythia [42], Herwig [43] or Sherpa [44]. In general, the full experimental description of a physics channel, requires the simulation of many different processes, as an example, the background and the signal generation. A typical hadronic process simulation starts from Lagrangian models and matrix elements: the first step is the calculation of the probability for quarks and gluons to produce the parton shower. The next step is

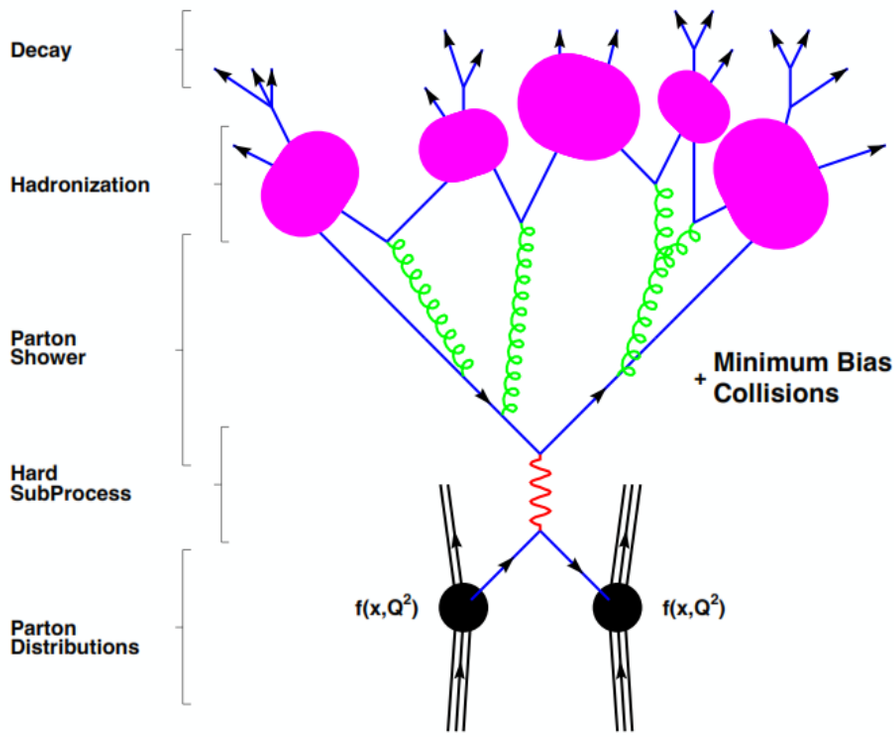

Figure 2.10: Schematic view of the typical hadronic event generation process.

the simulation of the hadronization process: colourless hadrons originate from the coloured partons produced in the shower. The last step of this chain is the simulation of the hadron decay chains towards lighter and more stable states.

After the generation, the events are passed through the simulation of the interaction with the detector material, such as energy loss and scattering. The most important toolkit for detector geometry simulation is GEANT4 [45]: it provides a detailed description of the detector response to the particle interaction, taking into account also the presence of magnetic fields.

Event reconstruction and analysis

The simulated events generated in this way are completely compatible with real data collected by the detector: the reconstruction algorithms can operate both with simulated and real data. During this step, multiple tasks are performed: pattern recognition, track fitting, vertex determination, energy and momentum measurement. Finally, real data and Monte Carlo simulations are used to perform comparative analysis between experimental results and theoretical prediction. Many different analysis tecniques are used to look at data from different perspectives. Usually the analysis consists in software programs in C++ language implemented on ROOT [46, 47] software, with additional dedicated libraries, such as RooFit [48].

Chapter 3

Tracking detector technology

The LHC accelerator is going to be upgraded to High-Luminosity LHC (HL-LHC): the instantaneous luminosity will reach 5 to 7 $\cdot$ 10^{34} cm^{-2} s^{-1}, with a pile-up at the level of 200 interactions per crossing. The LHC should conclude the first part of its physics program at the end of 2023 (see Figure 3.1) with an integrated luminosity for proton-proton collisions of 300 fb^{-1}. HL-LHC, with its expected integrated luminosity of 4000 fb^{-1}, will be able to maximize our understanding on SM and maybe it will open new physics scenarios beyond the SM. The ATLAS detector will be upgraded too, in order to cope with the HL-LHC environment. In particular, the current tracking detectors will be completely replaced by a new silicon detector with increased granularity and radiation hardness: the Inner Tracker (ITk) [49, 50].

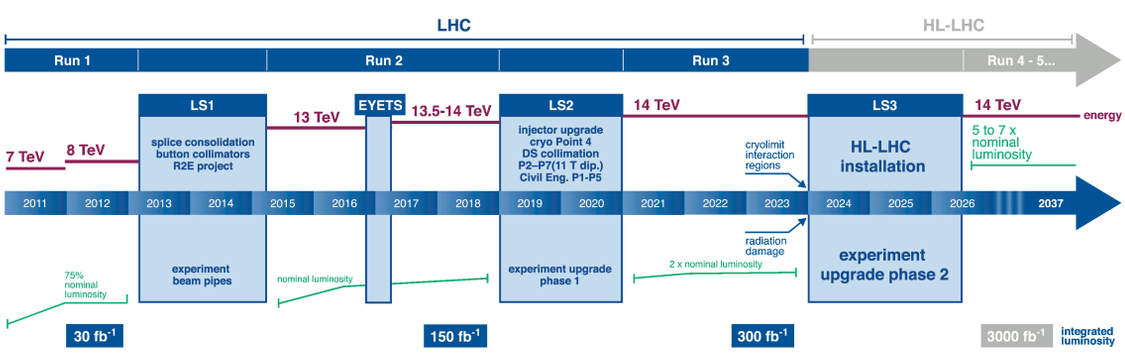

Figure 3.1: LHC physics program will end in 2023, the HL-LHC accelerator will follow.

Tracking and vertexing detectors are essential tools for the study of many phenomena at LHC, since many physics analyses depend on a precise tracking performance. In many cases, the tracking is performed using solid state detectors. In particular, one of the leading edge technology used for tracking and vertexing is the pixel silicon detector. To better understand the contribution I made to the field of future pixel detectors (described in Chapters 4 and 5), which are part of the efforts made in the design and prototyping of the ITk pixel detector, an introduction to the silicon tracking detectors technology is given in this Chapter, along with a brief description of the ITk detector layout.

3.1 Semiconductor detectors

When a charged particle (e.g., electron, pion or proton) penetrates into matter, it interacts with the electrons and nuclei present in the material through the electromagnetic force. Charged particles are sources of electromagnetic fields: a charged particle passing in the neighbourhood of an atom interacts electromagnetically with it as a whole, generating a state excitation or an ionization. More in general, a particle penetrating into a detector produces a uniform ionization along its path. As an example, about 23000 electrons are generated inside a 300 μm thick silicon layer. Actually, in the field of semiconductor detectors, the information carriers are electron-hole pairs, which are produced along the path taken by the charged particle through the detector.

By collecting electron-hole pairs, the detection signal is formed. One of the main advantages of using semiconductor materials instead of gas, is that they require lower energy to produce an electron-hole pair with respect to ionization chambers (3.6 eV for silicon versus 26 eV of argon gas). The mainly used semiconductor is silicon, since it is very cheap and can be found in great abundance. Other semiconductor materials are being investigated (e.g. diamond) which might offer better radiation hardness than silicon, even if they are not currently available in large samples or their performance is not yet as good.

Silicon, as every other semiconductor, has a forbidden region in the energy band structure, the band gap. The amount of free electrons in an intrinsic semiconductor (always equals to the amount of free holes) at ambient temperature (T = 300 K) is of the order of 10^{10} cm^{-3}. The silicon generally shows a low intrinsic conductivity that must be artificially increased in order to be used in devices. Therefore, additional states are inserted in the forbidden band gap so that a lower energy is required for hole or electron excitation. This procedure is known as "doping".

Silicon has four valence electrons and it is located in the IV Group of the periodic table. In order to modify its conductivity, usually elements from III Group (i.e. boron) or V Group (i.e. phosphorus, arsenic), having respectively one valence electron less (p-type) or more (n-type) than silicon, are used. The latter ones release their extra electron easily into the conduction band and are therefore called donors. Donor levels are very close to the conduction band. In turn materials from III Group are called acceptors as they accept the extra electrons from silicon.

The passage of a charged particle into the typical silicon detector would induce a signal of $2 \cdot 10^4$ electrons, which is very little compared to the larger number of free charge carriers (10^{10} cm^{-3}). Therefore, it is fundamental to reduce them by several orders of magnitude. This is obtained using p-type and n-type doped silicon in combination in a reverse-biased configuration (pn-junction). The reversely biased pn-junction is the basic element of the silicon sensors.

In the junction between the n-doped and p-doped materials, some of the charge carriers will diffuse from one side into the differently doped side. They will then

recombine with the majority carriers producing a region close to the junction which is depleted from free charge carriers. In the vicinity of the junction, donor and acceptor ions are left without their balancing charges, causing this region to be electrically charged with an electrical field counteracting the diffusion. An external voltage applied in the same direction of the electrical field would remove majority carriers from either side and extend the depleted region.

A simple semiconductor diode with only two electrodes can only detect the passage of a particle, but not its position. This information can be obtained by the segmentation of one or both electrodes. There are three main segmentation geometries, shown in Figure 3.2:

- Single side strip;
- Double side strip;
- Pixel.

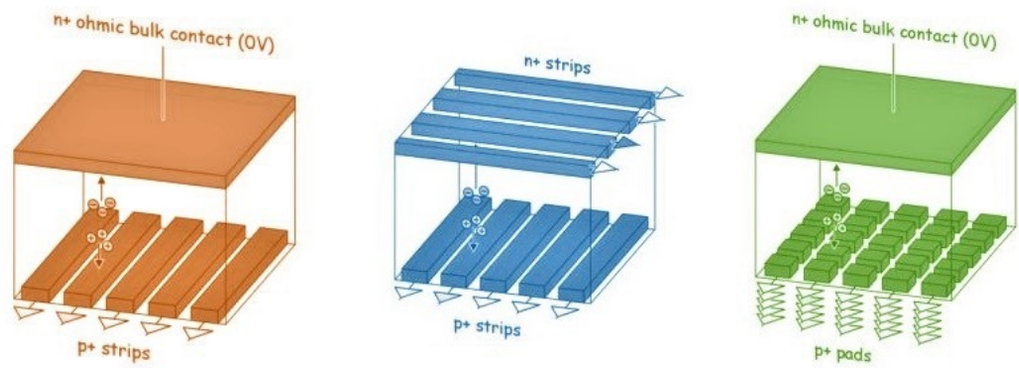

Figure 3.2: Single side (left) and double side (center) strip detectors, along with pixel detectors (right).

A strip detector has (single or double) strip-like implants acting as charge collecting electrodes, while pixel detectors are segmented in both directions. A single sided strip detector can provide only a one dimensional position information. To have a two dimensional position information, both electrodes have to be segmented into non parallel strips. The space resolution improves with a finer segmentation. In the last decades, the total surface and the segmentation level of the tracking and vertexing detectors have increased in order to cope with the increasing track densities due to higher luminosities of colliders. The main limitation to the pixel size usually comes from the electronics, because a large amount of circuitry must be fit in a single read-out pixel.

In trackers and vertex detectors several layers of pixel and strip detectors are used together to reconstruct the tracks of charged particles. Pixel detectors comes with better resolution (and reduced tracking identification ambiguity) but are more

expensive, therefore they are usually used only for the layers closer to the collisions, because of the higher track density.

3.2 Pixel detector technology

Three main different types of pixel detectors may be identified:

- Hybrid pixel detectors: The pixels of the sensor are connected to the Front-End (FE) readout chip through small solder bumps (see Figure 3.3). This technology has many advantages as high radiation hardness and good spatial resolution. The production of an hybrid detector is complex and laborious (involving bump-bonding and flip-chipping processes), as well as expensive. Another disadvantage is the higher material budget.

- Active hybrid pixel detectors: The so-called semi-monolithic detectors, currently under investigation, are still hybrid detectors. In case amplifier stages are implemented in the sensor, the signal size is sufficiently amplified to use different interconnection options, like capacitive mediums (i.e. a glue layer).

- Monolithic pixel detectors: It is possible to integrate parts or the entire electronics in the sensor, obtaining the so-called monolithic detectors. They are the standard devices for the detection of visible light. They are not being used yet in high energy physics due to the slower readout speed and the lower radiation tolerance. A considerable effort is being performed by the silicon detector community to produce and test prototypes that overcome these difficulties. The main advantages of such detectors would be lower production costs, easier assembly and integration.

In the ATLAS Pixel detector, as well as in the IBL, the hybrid pixel detector technology has been used. This technology is the preferred one for the ITk pixel detector too. Nevertheless, there is the possibility to have the external layer (the largest and the more expensive one) done in monolithic pixel technology, in case the prototypes are found to be compatible with the technical specifications. The following Sections are focused on the components of the typical hybrid pixel detector (the readout chip and the sensor) and on the hybridization technique.

3.2.1 Detector readout

The sensor converts the energy deposited by a particle to an electrical signal. This signal is processed by the electronic readout chain that can be located in the same piece of silicon (monolithic approach) or in a different tile of silicon (hybrid approach). The readout electronics usually consist of an analogue part to amplify and shape the signal and a digital data processing logic.

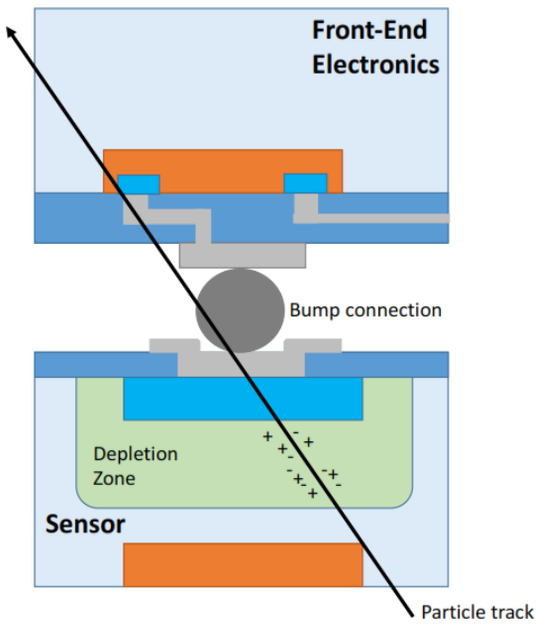

Figure 3.3: Section of a pixel cell after hybridization with a solder bump: the sensor at the bottom (for signal generation), the bump connection in the middle (for the interconnection) and the readout electronics (for the signal amplification and data processing) are shown. When a ionizing particle crosses into the sensor, it generates charges that move in the depletion region under the action of an electric field producing the signal.

As shown in Figure 3.4, the first two basic blocks of the typical front-end are the pre-amplifier and the shaper. The pre-amplifier is needed since the signal charge can be small, in the order of $4 \cdot 10^{-15}$ C. After the amplification stage, a pulse shaper is situated, that is basically a band-pass filter to improve the signal-to-noise ratio. Following the readout chain, the threshold discriminator is found: a discriminator compares the shaper output to a threshold value which is distributed globally to all pixels. Usually the threshold is set to low values in order to maximize the detection efficiency, but high eneough to keep the rate of noise hits at an acceptable level. Finally the discriminator output signal is routed to the digital readout chain where the hit information is stored in buffers. In the case of ATLAS pixel modules, the hit information stored consists of a time-stamp to associate the hit to the correct LHC bunch crossing, the pixel address and the digitized Times over Threshold (ToT) information.

3.2.2 Detector sensor

The most common sensor technologies among the hybrid detectors are show in Figure 3.5: planar (left) and 3D (right) sensors.

Planar sensors are the oldest technology, with proven radiation hardness and well established mass production capabilities. The pixels are obtained through the

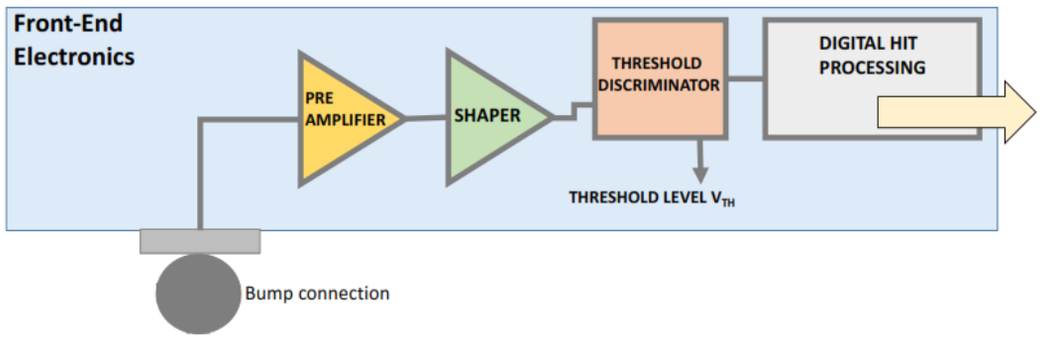

Figure 3.4: Steps of the typical readout chain of a hybrid pixel: the low-level signal, coming through the metallic bump from a pixel sensor cell, is integrated in a pre-amplifier, then fed to a pulse shaper. If the collected charge is higher than a predefined threshold level, the signal is digitized.

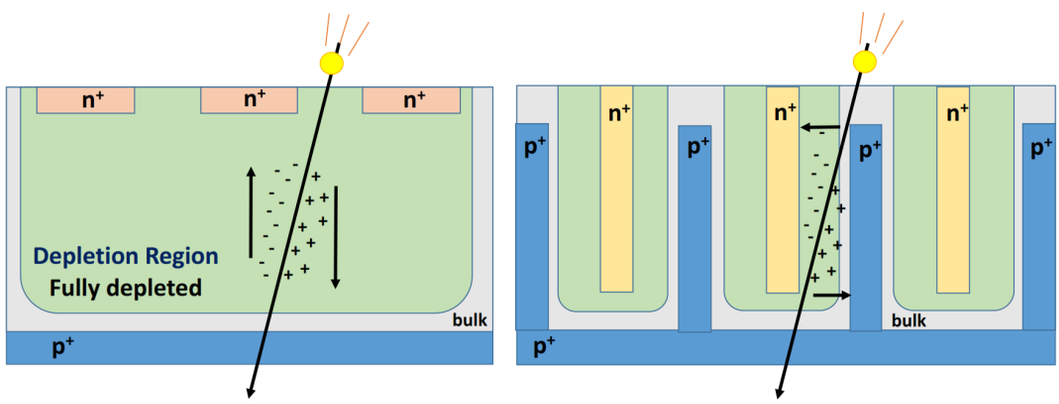

Figure 3.5: Structure of planar (left) and 3D (right) silicon sensors.

segmentation of one of the two electrodes. Planar sensors are made with $p-in-n$ or $n-in-n$ sensor. In Figure 3.5, the cross section of a $n-in-p$ pixel silicon detector is reported with the drift of charge carriers generated by an ionizing particle inside the depleted region.

The 3D sensors architecture was proposed for the first time in 1996 [51]. They are characterized by cylindrical electrodes perpendicular to the surface and etched into the bulk material. To realize this kind of structures micro-machining processes are used. Different processes (single side or double side) have been studied.

The 3D concept preserves the bulk thickness for charge generation while reducing the electrode spacing. In the 3D sensor, the same amount of charge of a planar sensor with the same substrate thickness is generated by a crossing particle. The main difference between the two technologies is that for planar device the inter-electrode distance is equal to the wafer thickness, instead for 3D detectors the distance can be optimized and it is possible to reduce it to very low values (less than 50 µm). Compared to planar detectors, the benefits regarding radiation damage are a shorter drift length for the charge carriers and therefore a much decreased depletion voltage.

3D sensors require a relatively low depletion voltage even after high irradiation dose, but are currently more expensive due to the more complex production processes.

3.2.3 Hybridization technique

Finally the sensors and the electronics are put together to form the hybrid module. Through the bump-bonding and flip-chipping process, each pixel of sensor is connected to the corresponding FE chip. The interconnection between chip and sensor is usually based on soldering, thermo-compression bonding and adhesive bonding. Many different bump metallurgies are used ranging from pure Au, Cu, Sn and In to alloys such as eutectic or high-melting PbSn, AuSn, AgSn, SnCu and AgSnCu, depending on the application. Concerning pixel detectors, two main technologies are well established and developed: electroplated solder bumps or indium bumps deposited by evaporation. The bump deposition is performed at wafer level, instead the flip-chip process is normally carried out on single dices.

Finally, the bare modules (sensor plus front-end chip) are glued to a flex hybrid circuit, which is wire-bonded to the front-end chip. The flex hybrid houses all passive components that are required to operate the front-end chips, like filter capacitors and resistors, and provides the high voltage connection to the backside of the sensor. A pigtail with a connector is used to connect each module to the electrical services of the detector.

3.3 ATLAS tracking detector upgrade

The ATLAS Inner detector was designed for 10 years of operations at the design instantaneous luminosity ($1 \cdot 10^{34}$ cm^{-2} s^{-1}, 23 inelastic proton-proton collisions per bunch-crossing). The specifications for radiation tolerance of the current detectors are significantly below to the 4000 fb^{-1} that will be collected at the end of the lifetime of the HL-LHC.

During Long Shutdown 3 (2023-2025) the Inner detector will be removed (both TRT and silicon trackers) and it will be replaced by an all-silicon tracker which fills the existing tracking volume, with pixel sensors within a radius of 362 mm around the beamline, surrounded by microstrip sensors outside of this radius. The ATLAS Inner detector has a pseudorapidity coverage of $|\eta| < 2.5$. The ITk detector will have a coverage of $|\eta| < 4.0$.

Many of the interesting phenomena at the HL-LHC includes jets in the final state. This requires the tracker to cover large pseudo rapidities up to $|\eta| = 4$, to reject pile-up jets through the jet-vertex-association. Despite the significantly higher track density at the HL-LHC with respects to the LHC, the occupancy of the tracking detector needs to be kept at low levels in order to facilitate efficient tracking with a good vertex resolution. This will be achieved by reducing the pixel size significantly with respect to the current Pixel detector. Each pixel will have a

size of either 50×50 μm^2 or 25×100 μm^2 (ATLAS Pixel detector: 50×400 μm^2; IBL detector: 50×250 μm^2).

The layout of the ITk is being finalised. In particular, the ITk pixel detector will consist of 5 layers of modules (see Figure 3.6), which are arranged in three different sections per layer. In the low $|\eta|$ region, the modules are placed in parallel to the beam axis (flat section), while in the high $|\eta|$ region (endcaps) they are placed perpendicular to the beam axis. In the intermediate $|\eta|$ region, the modules will be tilted at an angle with respect to the beam axis (inclined section). The detector will be made by a total of about 10000 hybrid pixel modules, with thin planar sensors in the outermost layers and 3D sensors in the innermost layer. Due to the large number of modules and the high current consumption of the front-end chips, a parallel powering scheme for the modules is not reasonable. A serial powering scheme will therefore be deployed in the ITk pixel detector, with up to four front-end chips per module powered in parallel and up to 13 modules connected in series.

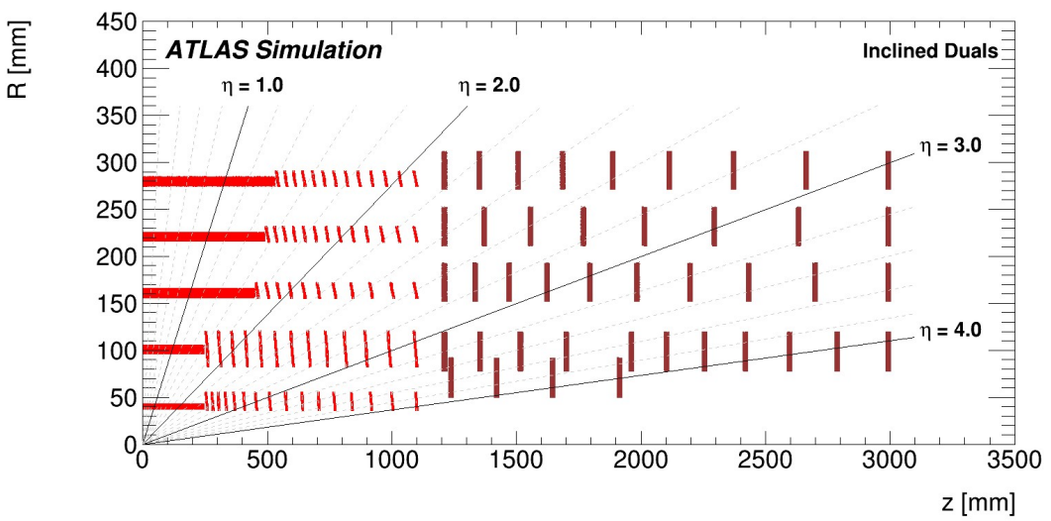

Figure 3.6: Possible layout of the ITk pixel detector with five layers. The layout provides a hermetic coverage for tracks with a pseudo rapidity of up to $|\eta| < 4.0$. Each layer is divided into three sections, a flat section, an inclined section and the endcap rings

The new ITk detector should operate under high fluencies (a NIEL[1] up to $1.4 \cdot 10^{16}$ n_{eq} cm^{-2}), with a correlated high radiation damage. The ITk pixel detector is being designed to sustain a Total Ionizing Dose (TID) of 1 GRad, while the ITK strip detector about 50 Mrad: a lower radiation tolerance is needed for the Strip detector, since it will be farther than the Pixel detector from the interaction point and it will receive a lower amount of radiation. The radiation level of the ITk pixel detector in terms of 1 MeV n$_{eq}$ fluence and TID is shown in Figure 3.7.

[1]NIEL: Non Ioninizing Energy Loss, where 1 MeV n$_{eq}$ is the number of particles with a non-ionizing energy loss of a 1 MeV neutron.

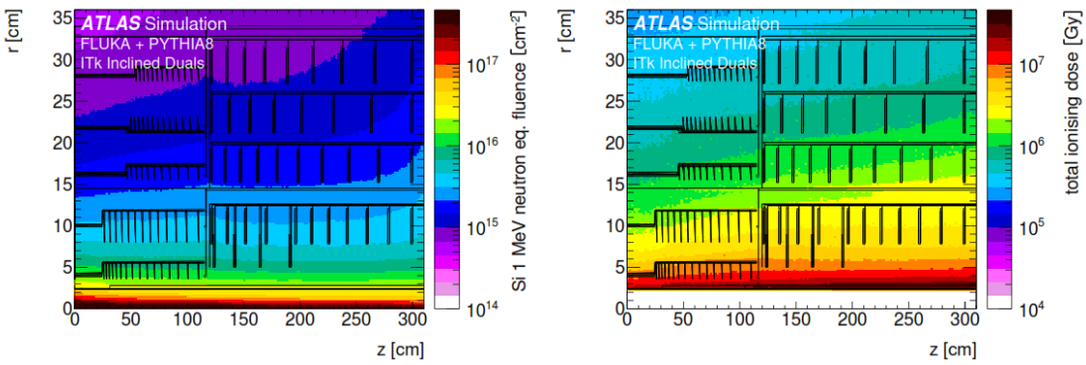

Figure 3.7: ITk pixel detector simulation of radiation level at HL-LHC (4000 fb^{-1}) in terms of 1 MeV n_{eq} fluence (left) and total ionising dose (right).

The pixel detectors modules need a completely new design in the readout electronics, sensors and interconnections. A new 65 nm front-end electronics is being developed by the RD53 collaboration, in a joint effort between the ATLAS and CMS experiments. It will be compatible with smaller pixel sizes than the actual ones to cope with the higher track densities. The ATLAS chip will consist of a pixel matrix of 400 × 384 pixels. The expected data rates are as high as 5.12 Gbits/s per front-end, being transmitted over up to 4 AURORA lanes running at 1.28 Gbits/s per chip.

The hybrid pixel modules consist of one to four readout chips bump-bonded to a silicon sensor, where each front-end chip has a size of roughly 2×2 cm^2. The innermost layer, Layer 0, will consist of single chip modules with 150 μm thick 3D sensors. Layer 1 will consist of quad chip modules with 100 μm thick planar sensors, and the outermost layers will consist of quad chip modules with 150 μm thick planar sensors.

The sensor prototypes show a hit efficiency of more than 97% after irradiation to 10^{16} 1 MeV n_{eq} at bias voltages of about 400 V / 600 V for the 100 μm / 150 μm thick planar sensors, and below 200 V for the 3D sensors.

The local suppors of the ITk Pixel Detector will be made of low mass carbon structures with thin titanium pipes for CO_2 cooling. In the inner system, the flat section will consist of staves with a single cooling pipe, while there are several different designs for the rings in the innermost two layers: stand-alone rings for L0 and L1; while for the intermediate $|\eta|$ region, coupled rings with single chip modules in the inner ring and quad chip modules on the outer ring. In the outer layers, the endcaps and the inclined section will consist of half-rings, where modules are mounted on both sides to allow the complete coverage of the azimuthal angle, sharing a common cooling pipe per half-ring. The low $|\eta|$ region of the outer layers will be made by "longerons", carbon truss structures with two coolings lines, supporting two rows of modules which are slightly tilted with respect to each other.

While the final version of the readout chip for the ITk Pixel Detector is not yet

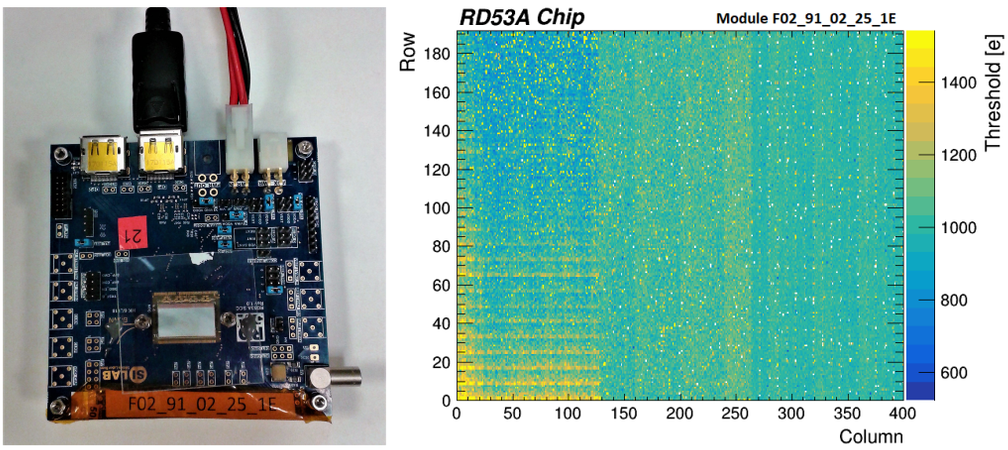

Figure 3.8: First RD53A chip module prototype assembled in the ATLAS Genoa lab on the Single Chip Card (left) and its threshold map (right), after tuning the discriminator values to 1000 electrons.

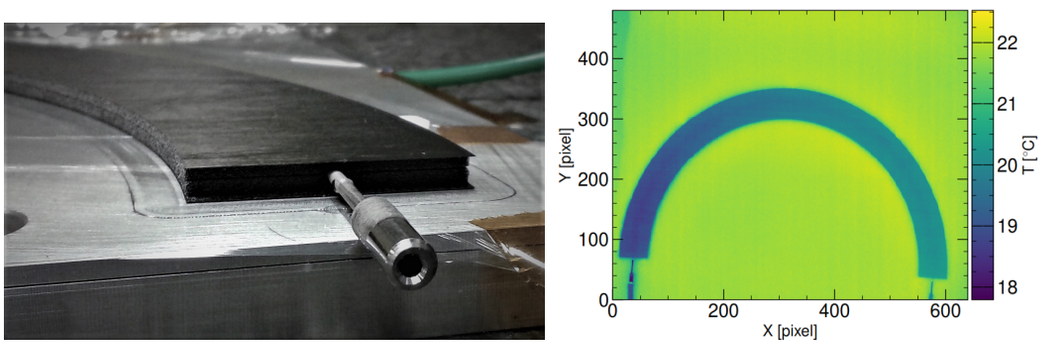

Figure 3.9: Detail of the titanium cooling pipe of the first half-ring prototype assembled in the ATLAS Genoa lab (left) and the thermal profile of the half-ring (right), after the injection of cold water inside the cooling pipe.

available, an extensive prototyping campaign for assembling modules has started to demonstratate several aspects of the new detector layout. Prototypes of local supports have been produced as well, to validate their mechanical properties and thermal performance.

I am currently involved in this effort, within the activities of the ATLAS Genoa group. I am testing in laboratory the first ITk modules prototypes assembled in Genoa (see Figure 3.8), built with 3D sensor connected to the RD53A chip. I am participating to the test beam campaigns, where these modules are tested, before and after irradiation, to measure the hit detection efficiency. I am performing as well thermal tests of the first end-cap half-ring prototypes assembled in Genoa (see Figure 3.9). Since I joined these activities recently (beginning of 2019) and everything is still ongoing, I have not documented them in this thesis.

Chapter 4

Wafer Level Packaging technology

Even for the ATLAS experiment, equipped with a complete and funtional detector, the R&D is still an important reality. With the perspective of accelerator upgrades, the research community continues to develop technologies and instruments for future detector components. This has the double goal of improving the performance and mantaining the reliability in harsh environments. Wafer Level Packaging (WLP) is a process developed with the goal of rebuilding a wafer structure starting from previously diced tiles. The aim is to exploit this technique to build larger silicon detectors, reassembling good tiles on a full wafer. Many of the processes involved in the silicon detector module assembly involve steps that are preferably performed at the wafer level to speed up the production (i.e. the bump-bonding and flip-chipping processes). Six wafers were produced with the WLP technique by MicroFab Solutions in Trento within the AIDA-2020 project [52] (as part of the Horizon 2020 european project). The WLP project defined in collaboration between MicroFab Solutions and the INFN Genoa group was focused on the production of wafers with certain standards (thickness, planarity, placement accuracy) compatible with the production of Pixel modules for high energy physics applications (e.g. ITk detector).

After a brief introduction to the AIDA-2020 activities (Section 4.1) and to the motivation of the development of the WLP technology (Section 4.2), the technical details of the process flow are presented in Section 4.3. The wafers produced by the MicroFab Solutions are presented in Section 4.4. I have performed the measurement of their properties in terms of planarity and tiles placement accuracy. The results are presented in Sections 4.4.1 and 4.4.2, respectively.

4.1 AIDA-2020

The AIDA-2020 Advanced European Infrastructures for Detectors at Accelerators project has received funding from the European Union's Horizon 2020 Research and Innovation programme under Grant Agreement n. 654168 [52]. In total, 24 countries and CERN are involved in a coordinated programme in line with the priorities of

the European Strategy for Particle Physics. Fifteen different tasks (namely Working Packages, WP) are defined within the AIDA project. The Wafer Level Packaging is part of the WP 6, toghether with CMOS active sensors developments.

The main goal of WP6 is to develop novel High Voltage and Resistive (HV/HR) CMOS active sensors for high energy physics applications. Within the WP 6.4 activities, hybridization procedures between depleted CMOS sensors and state-of-the-art readout tiles were investigated. Active CMOS devices can be monolithic, where sensor and electronics are placed in a single substrate, or can be used in hybrid devices, where the active sensor and the readout electronics are two separate substrates interconnected with solder bumps (bump-bonded devices, see Figure 3.3) or through capacitive coupling. The hybridization process is technically demanding since the pixel size is extremely small (tens of micro-meters). The aim of the WP 6.4 activities is to investigate and develop technical solutions for the hybridization procedure, both for capacitive coupled and bump-bonded devices. In both cases the hybridization step requires precise alignment between the active sensor and the tile, so that each pixel is connected.

The capacitive coupling techniques were studied extensively by the INFN Genoa group in collaboration with the University of Geneva. In this case, the coupling is performed gluing both substrates with various glues using a precise pick-and-place process. Several glues (including tape) were investigated for the interconnection. Studies indicated difficulties in achieving uniform capacitive coupling across all the pixels. The use of pillars to aid the hybridization process improved the uniformity of the capacitive coupling. HV/HR CMOS structures developed within the AIDA-2020 project (as part of the WP 6.3 activities) were used as active sensors and interconnected to the readout chip. Several technical difficulties regarding the fabrication process were overcome and assemblies were produced and tested in different institutions.

It should be noted that to industrialize the capacitive coupling procedure a wafer level process would be desirable. With this in mind, the WLP technology was investigated at MicroFab Solutions in order to rebuild wafers from good tiles and carry out the capacitive coupling process at wafer level.

4.2 Motivations and specifications

Wafer Level Packaging is a rather recent technique [53,54] with different applications in many fields of semiconductor technologies [55]. One of the goals of performing WLP in high energy physics is to handle the case of wafers with low yield of working tiles, reassembling good tiles on a full wafer. After rebuilding the wafer according to certain criteria, it is possible to carry out wafer processes (i.e. bump-bonding). Another example is to exploit the WLP to build larger detectors, assembling modules in structures for easier handling and loading on supports.

The WLP process developed at MicroFab Solutions is intended for sensors and

tiles to be used in particle detectors for high energy physics applications. The rebuilt wafers should respect some conditions in order to be usable for wafer processes intended for tracking detectors:

- thickness: thinner tiles (and wafers) have a lower radiation lenght, being therefore more transparent to particles (less scattering and lower energy loss by particles in tracking detectors);
- planarity: the overall planarity and the maximum bowing of the rebuilt wafer are required to be minimal, within technical specifications of wafers to be used for wafer processes;
- tiles placement: in order to perform wafer processes on pixel cells (dimension: tens of microns) a high accuracy in tiles placement is required.

During the R&D process of the WLP technology, the specifications for wafers used in IBL production were taken into account (planarity better than 10 µm and bowing less than 60 µm) along with the needs for ITk pixel modules production (sensor thickness between 150 μm and 300 μm). The tiles placement precision needs to meet the standards for hybridization: bump deposition processes (bump-bonding) and sensor to front-end chip matching (flip-chip). Due to the high track density in HL-LHC environment, the segmentation of the pixel sensors will increase (from 50×250 μm^2 of IBL pixels to 50×50 μm^2 or 25×100 μm^2 of ITk pixels) and the bump density will reach up to $4 \cdot 10^4$ bumps per cm^2. The tiles placement accuracy needed for hybridization processes is estimated to be about 1 μm.

4.3 Process flow

The WLP process consists of 4 different steps (see Figure 4.1): lamination, tiles placement, molding and de-bonding. The process is performed inside a mold cavity, where high temperatures and pressures are applied.

The first step of the process, the lamination, consists in the application of a thermal release tape on a carrier, in order to protect the electronic components. The carrier is a support wafer which is placed inside the mold cavity. It is possible to regulate the thickness of the final wafer (to produce thinner wafers), by using carrier wafers with different thickness. The choice of the tape is fundamental for the last phase of the process, when the tape is removed from the rebuilt wafer. The use of a carrier facilitates the tiles placement phase: the tiles are placed on the tape by using patterns for the alignment (see Figure 4.2).

Once the carrier is filled with tiles, the compression molding can start. The molding material (a resin) is placed in an open mold cavity (where the tiles were placed). The mold is closed with a top controlled force while heat and pressure are maintained until the molding compound has cured. Then the mold is removed and the molding material is heated (foaming).

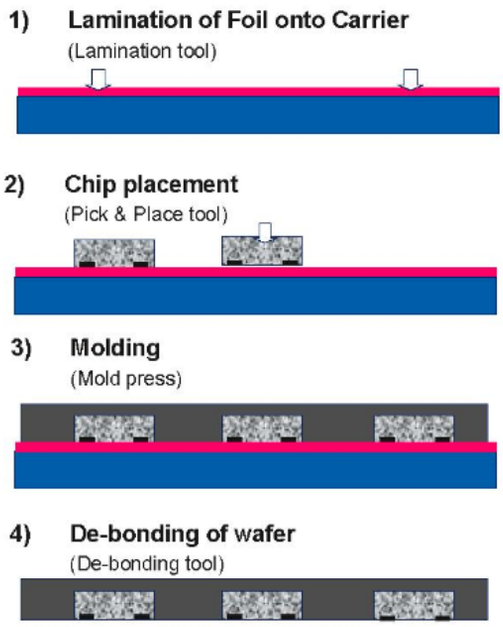

Figure 4.1: Steps of the Wafer Level Packaging process.

Finally, the carrier and the tape are released (de-bonding or peeling, Figure 4.3). The carrier-tape removal operation is a very delicate process, in fact this is the phase with the highest risk to damage the final wafer: the thinner the wafer, the higher is the risk to damage it. The tape-resin combination choice deeply affects the structural integrity of the wafer during the peeling phase. Moreover, the material used in the molding process should be coherent with the tiles material (silicon) and resistant to the handling. After removing the carrier and the tape, the wafer is ready to perform wafer-to-wafer bonding processes.

4.4 Wafer production and test

Six 6-inch wafers were produced by MicroFab Solutions in Trento with the WLP process, their properties are resumed in Table 4.1: two different filling schemes were used (full or cross, see Figure 4.4) for three different wafer thickness values (675 μm, 400 μm, 300 μm).

Wafer	Thickness [μm]	Filling scheme
1	675	cross
2	675	full
3	400	cross
4	400	full
5	300	cross
6	300	full

Table 4.1: Properties of the six wafers produced by the MicroFab Solutions.

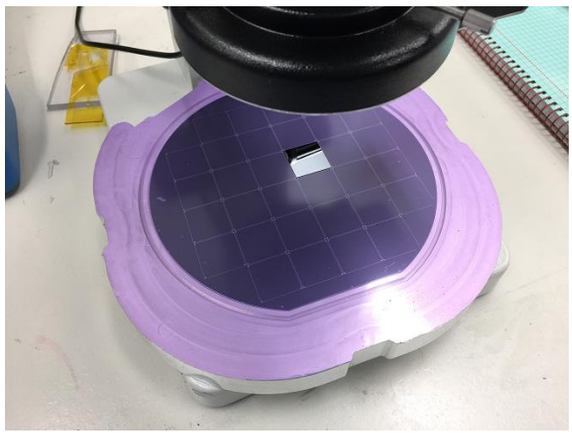

Figure 4.2: Carrier wafer during the placement phase: the first tile has been deposited on the tape.

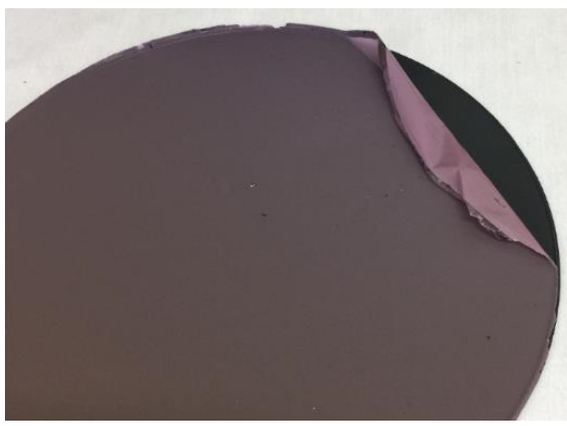

Figure 4.3: The tape is removed from the wafer.

The wafer production plan included 6 wafers. The thickness of the wafers have been reduced step-by-step, from 675 μm (1 and 2) to 400 μm (3 and 4) and then to 300 μm (5 and 6) confirming the solidity of the compound. The first production includes wafers of 675 and 400 μm, that are strong enough to be handled. The following production includes two more wafers with the minimum achievable thickness, 300 μm (the tiles used are 300 μm thick).

Two filling schemes were conceived in order to further test the strength of the resin. Wafer 1 and 2 are shown in Figure 4.4: wafer 1 has 32 tiles (full filling scheme) while the wafer 2 has 10 tiles (cross filling scheme). The resin used as molding compound is visible in black.

The WLP process was performed using an alluminum mold specially built for this applicaction. The mold is made of two engraved parts, a bottom side and a top side (see Figure 4.5). The carrier wafer is placed inside the bottom side of the mold, then the tape is added by lamination and the tiles placement is performed. The tiles used in this application are dummy chips of 300 μm thickness with alignement crosses. The machine used for the tiles placement has a precision of about 10 μm

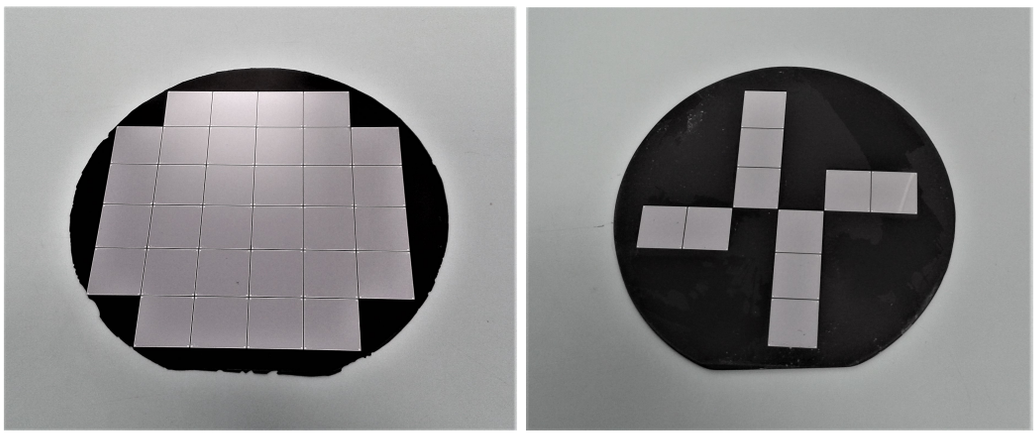

Figure 4.4: Wafer 1 (left) and 2 (right): they have a different filling scheme.

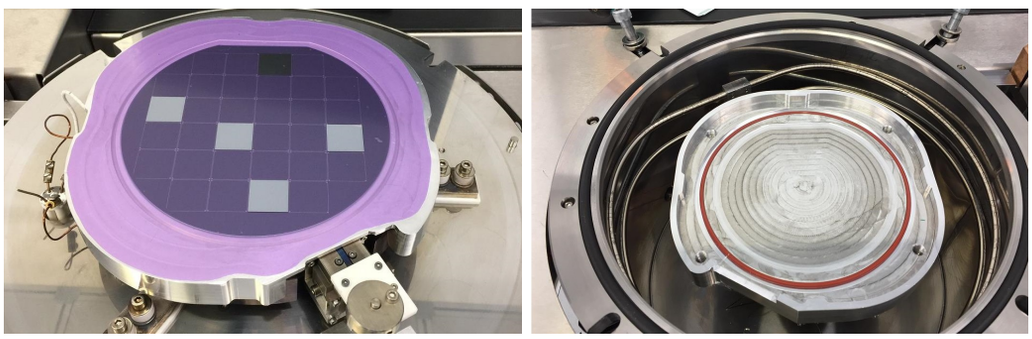

Figure 4.5: The mold is made of two engraved parts: a bottom side (left) and a top side (right).

in the positioning of the tiles, while a typical pick-and-place machine can reach a precision of 0.5 μm.

The molding material used in this application (XV5791S14 Panasonic resin) is made by 81% Silicon with maximum fragment size of 5 μm. The tape (Nitton) used during the production of wafers 1 to 4 is visible in purple in Figure 4.2. Wafer 3 was damaged due to the force applied during the tape removal (see Figure 4.6): the pressure applied has broken twice the resin on the line of separation between tiles. The last two wafers (5 and 6) were produced with a different tape recommended by Panasonic to be compatible with the resin. The new tape has managed to improve the tape removal process.

4.4.1 Planarity measurements

The wafers were sent to the INFN Genoa labs in order to measure their planarity and the precision of the tiles placement. I have performed profile measurements, with a one point per μm precision, to extrapolate the planarity of the wafers. Several measurements were performed with a KLA P-7 mechanical profilometer, on both sides of the wafers (front and back) and on both directions (X and Y axis).

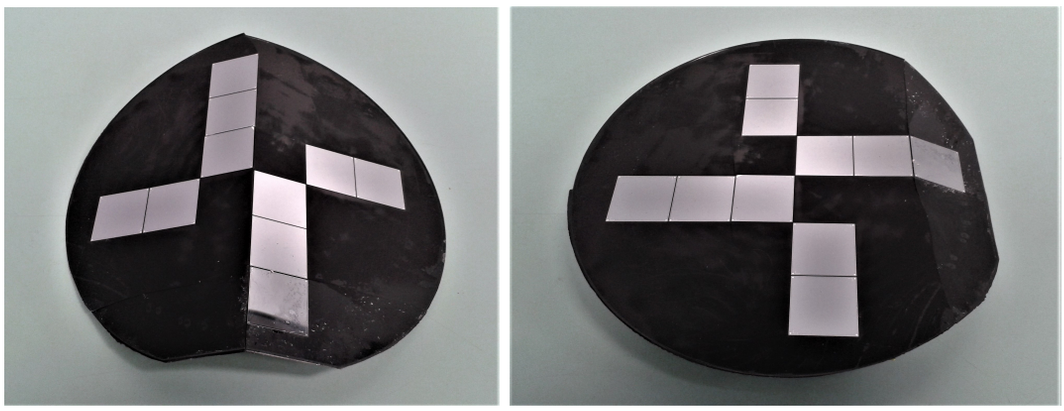

Figure 4.6: Wafer 3, damaged during the tape removal.

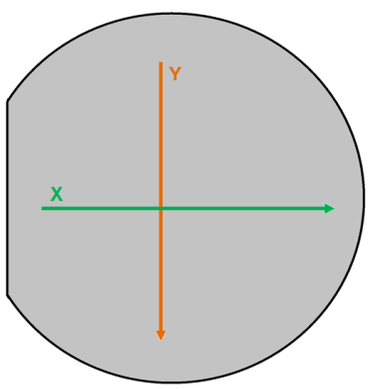

Figure 4.7: Example of X and Y axis profile measurement on wafer.

The results of the profile measurement of the three wafers with the full filling scheme are presented in Figure 4.8. The profiles of wafers 2 (675 μm thickness, red line) and 4 (400 μm thickness, blue line) show a bending point in the separation line between two tiles, visible in both X and Y profiles. The wafer 6 profiles (300 μm thickness, orange line) does not present such a feature and the planarity is improved (overall bowing below 100 μm). The improvement is due to a different tape choice. The tape used for wafers 2 and 4 was hard to separate from the molding compound, therefore a high force was applied during the tape removal. The new tape used for the wafer 6 (easily detachable from the molding compound) avoided the formation of bending points and improved the planarity.

Several sequential measurements along X axis, with a 1 mm pitch along Y, have been taken on wafer 6. The 3D reconstruction of the central part of wafer 6 surface is shown in Figure 4.9: two bending lines are visible along X axis in corrispondence of the separation line between tiles, with a slight general deformation of the surface. The overall planarity of wafer 6 is close to the specifications required for IBL pixel modules wafers (planarity better than 10 µm and bowing less than 60 µm was required in IBL wafers): further improvements in the production techniques may result in wafers compatible with the acceptance criteria.

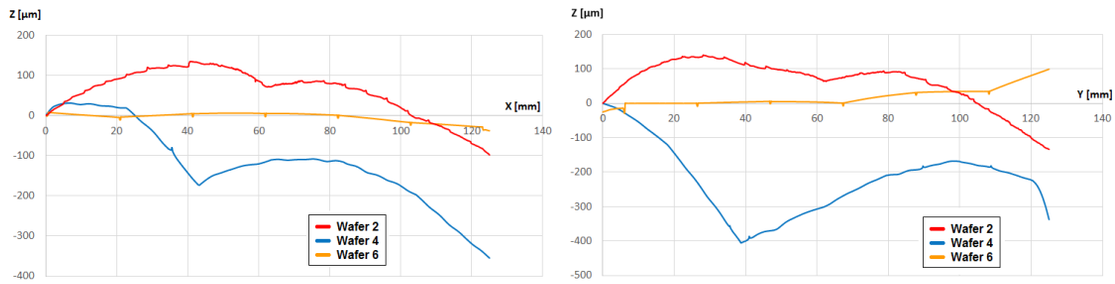

Figure 4.8: Profile measurement of wafers with different thickness (red: 675 μm, blue: 400 μm, orange: 300 μm). Profile X is shown on the left, profile Y on the right.

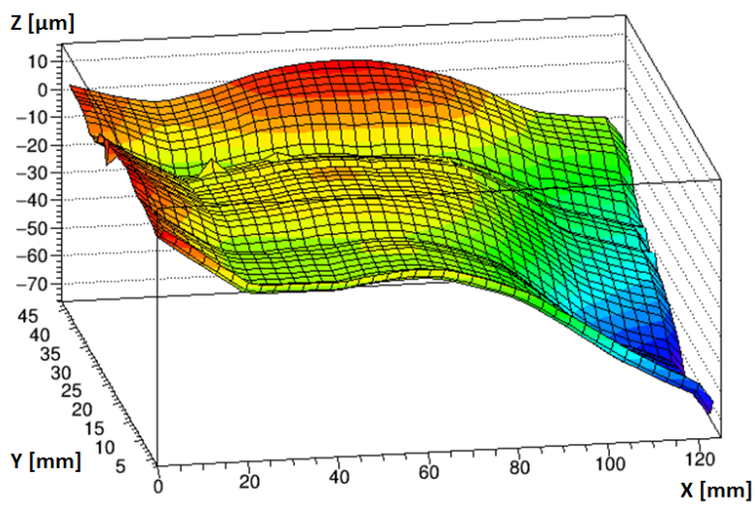

Figure 4.9: 2D reconstruction of the wafer 6 surface.

4.4.2 Tiles placement measurements

The placement of the tiles is performed with the help of alignment crosses: the crosses visible on the carrier wafer are used as reference to place the diced tile on the tape (see Figure 4.10). The cross of the tiles used in the rebuilt wafer are visible in Figure 4.11, the resin between the tiles is visible in black.

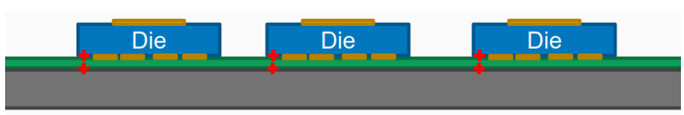

Figure 4.10: Sketch of the positioning of the tiles on the carrier wafer.

The profile measurements performed to assess the wafer planarity have been used as well to extrapolate the tiles placement accuracy. A detail of the profile measurement performed on the separation line between two tiles of wafer 4 is shown in Figure 4.12: the aligment crosses are visible (height: 0.80 $\pm$ 0.05 μm). It can

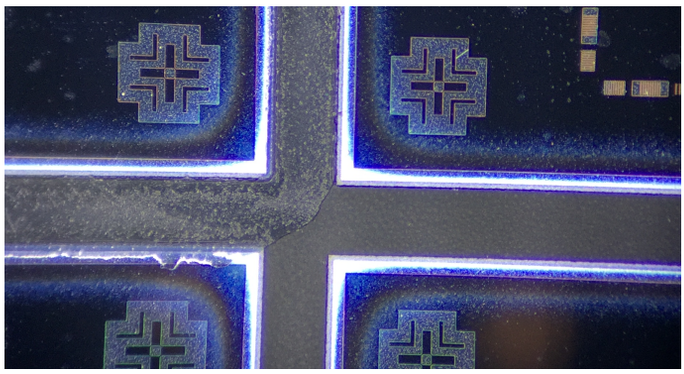

Figure 4.11: Corners of 4 tiles on the rebuilt wafer: the alignment crosses are visible.

be noted that the volume between the tiles is not fully filled by the resin: in many cases $\sim 10\ \mu m$ deep wells are observed in between (depth: $12 \pm 1\ \mu m$).

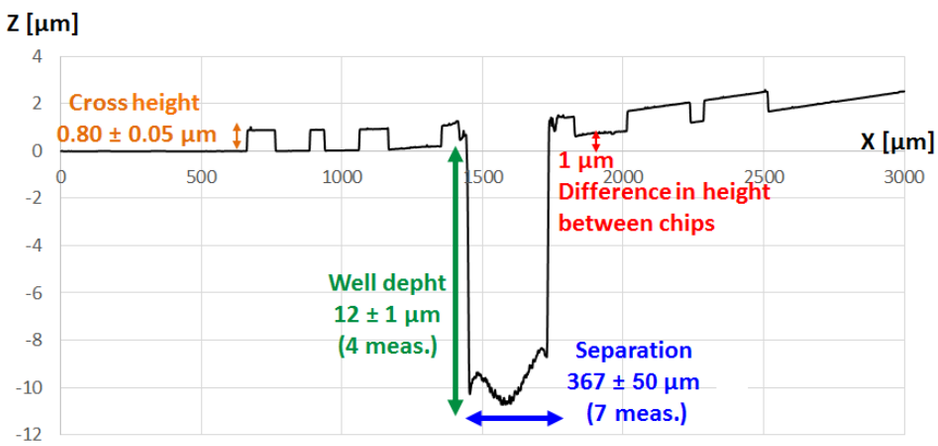

Figure 4.12: Detail of the profile measurement performed on the separation line between two tiles of wafer 4: a small depth well is found between the tiles (average depth: $12\ \mu m$), the alignment crosses of both tiles are visible (cross height: $0.8\ \mu m$).

The RMS of the wells width has been used to estimate the accuracy of the tiles placement achieved by the WLP process. It seems that the tiles placement accuracy has improved as well thanks to the new tape: the average distance between tiles in wafer 4 was found to be $367 \pm 50\ \mu m$ (7 measurements), while the average distance obtained with the same measurement performed on wafer 6 was found to be $336 \pm 10\ \mu m$ (5 measurements). The placement accuracy observed on wafer 6 is compatible with the precision of the machine used by MicroFab Solutions for the tiles placement. Therefore, it seems that the overall WLP process has no effect on the tiles placement accuracy. Nevertheless, the achieved accuracy is not yet acceptable for high precision processes like the bump deposition (a placement precision of at least $1\ \mu m$ is required for hybridization processes). It is therefore suggested to use a pick-and-place machine to obtain higher accuracy.

4.5 Outlook

The Wafer Level Packaging process has been developed within the AIDA-2020 project in a strict collaboration between the INFN Genoa lab and the MicroFab Solutions industry, with the aim to develop a process to be used to rebuild wafers from previously diced tiles, for the construction of large size silicon detector components with applications in the high energy physics field. This technology was investigated as a first step towards the industrialization of the process. During the R&D phase, precision measurements were performed in order to assess the properties of the output wafers with respects to the specifications and to eventually introduce solutions to optimize the process.

The six 6-inch wafers produced have been found to be strong enough to be handled, even in the case of the 300 μm thick wafers (the minimum achievable thickness). I have performed high precision profile measurements with a mechanical profilometer with the goal to assess the wafer planarity and the tiles placement accuracy. The measurements performed on the first four produced wafers highlighted the presence of bending points in the separation line between two adjacent tiles, due to the removal of the Nitton tape. Therefore, the process has been improved introducing a new tape, recommended to be compatible with the Panasonic resin. The wafer planarity has improved substantially: no bending lines are seen through the newly produced wafers. It seems that the tiles placement accuracy has improved too, thanks to the new tape.

The WLP process is close to meet the technical specifications required for wafers to be used in the wafer processing steps for silicon detector production. Further optimizations are required, as an example, it is recommended to use a pick-and-place machine for the tiles positioning in order to achieve the required accuracy. Small productions for future silicon tracking detectors may already profit from the WLP process, but not before having ascertained the functionality of real sensor and chip tiles obtained from wafers produced with this potentially destruptive production flow (involving high pressures and temperatures). In case of mass production for large area silicon detectors, a more detailed inspection of the output wafers is recommended, along with further tests that were not performed at this stage (i.e. relative thickness of the wafer, radiation hardness of the resin included in the wafer).

Chapter 5

Beam-loss scenario test beam

The ATLAS detector [9], and in particular the Pixel detector [32] which is the closest to the interaction point, is designed to sustain high dose integrated over several years of operation. The intrinsic radiation hardness of the silicon detectors should also favor the survival in case of accidental beam-losses. These events are very unlikely to happen since several systems (beam monitors, beam dumps, collimators, beam absorbers) are implemented to guarantee safe operations of the accelerator and of the experiments.

In 2006, an experiment [56] established that the pixel modules could survive to beam-losses as large as $1.5 \cdot 10^{10}$ protons/cm^2 in a single bunch of 42 ns, with minimal or no deterioration of performance. This measurement set a survival threshold well above the worst expected beam-loss scenario at the LHC.

During Long Shutdown 3, LHC will be upgraded to HL-LHC to reach higher instantaneous luminosity. The aperture of the HL-LHC quadrupoles in the proximity of the interaction regions will be larger with respect to the current LHC aperture. The aperture of the quadrupole absorbers (TAS) protecting the magnets from the collision debris will be larger too, from the current 17 mm radius to 30 mm radius, potentially exposing the ATLAS detector to a larger fluence of beam-induced radiation towards the interaction region.

The increased intensity of the collisions produced by the HL-LHC accelerator, together with the larger apertures, requires for new measurements of the beam-losses survival threshold for the tracking detectors, including both sensors and electronics. The components that are being developed for the ITk detector needs to be tested with high energy and intensity beams. The new damage thresholds need to be compared to the level of radiation received in beam-loss scenarios at the HL-LHC, to assess if they are able to survive and to quantify the performance degradation.

In 2017 and 2018, two experiments have been performed on recent silicon modules (IBL pixel, ITk strip) with an unprecedented high energy and intensity beam at the CERN HiRadMat facility. In this Chapter, after an introduction to the HiRadMat facility (Section 5.1), there will be the description of the beam operations (Section 5.2), of the tested devices (Section 5.3) and of the experimental apparatus

(Section 5.4) used in these experiments. Together with the Genoa group, I was involved in the activities regarding IBL pixel modules: the measurements performed on IBL modules will be presented (Section 5.5) along with the results (Section 5.6).

5.1 HiRadMat facility

High-Radiation to Materials (HiRadMat) [57] is a test beam facility at CERN, designed to provide a high-intensity pulsed beam to an irradiation area where material samples can be tested. The facility uses the high-energy 440 GeV proton beam extracted from the CERN Super Proton Synchrotron (SPS). Each pulse is made of 1 to 288 bunches (up to $1.2 \cdot 10^{11}$ protons per bunch) with 25 ns separation or higher, reaching a maximum pulse length of 7.2 μs. The proton beam can carry up to a maximum pulse energy of 3.4 MJ. The proton beam parameters are resumed in Table 5.1. In addition to protons, ion beams with an energy of 173.5 GeV/nucleon and a total pulse energy of 21 kJ can be used: up to now, no experiment has ever been performed with ion beams at the HiRadMat facility.

Proton Beam Parameters	Value
Beam Energy	440 GeV/c^2
Pulse Energy	up to 3.4 MJ
Bunch intensity	up to $1.2 \cdot 10^{11}$ protons
Number of bunches	1 to 288
Maximum pulse intensity	$4.0 \cdot 10^{13}$ protons
Bunch length	11.24 cm
Bunch spacing	25, 50, 75 or 150 ns
Maximum pulse length	7.2 μs
Cycle length	18 s
Beam radius at target	0.5 to 2 mm

Table 5.1: HiRadMat facility proton beam parameters.

Two separate parallel tunnels host the beam line with the experimental tables (TNC tunnel, Figure 5.1, left) and the read-out system (TT61 tunnel, Figure 5.1, right). Long connecting cables ($\sim$15 m) pass through a concrete screening wall placed between the TNC and the TT61 tunnels. They connect the experimental setup to the powering and read-out systems. Due to the high radiation level, it is not possible to control the setup neither from the TNC tunnel or from the TT61 tunnel: the operations of the modules are remotely controlled from the CERN Control Center.

HiRadMat is not an irradiation facility where large doses on equipment can be accumulated. It is rather a test area designed to perform single experiments in order to evaluate the effect of high-intensity pulsed beams on materials or accelerator components. The facility is open to CERN users and external groups, as all other

Figure 5.1: HiRadMat experimental area: TNC tunnel (left), hosting the beam line and the experimental table, and TT61 tunnel (right), hosting the powering and readout of the detectors.

experimental areas and test beams at CERN. The first experiments, performed in 2012, included candidate materials and prototype assemblies of LHC collimators foreseen to operate at the ultimate LHC beam powers, as well as beam windows and high-power target materials, such as tungsten powder.

The facility is designed for a maximum of 10^{16} protons per year, distributed among several experiments. This limit allows reasonable cool-down times for the irradiated objects (few months to a year) before they can be analysed in a surface specialized lab. A specific beam pulse list defined by each HiRadMat experiment is exploited during the beam operations. The experimental team decides when to shoot every pulse, according to the experiment recovery time but also to the availability of SPS beam time, which is shared with other users, i.e. for LHC fills.

5.2 Beam operations

ATLAS silicon modules have been exposed to the beam in the HiRadMat facility on July 2017 and on May 2018. Two different beam configurations were used during the test of the silicon modules: wide beam (2 mm radius) to test the global effects of the irradiation on a large part of the module and narrow beam (0.5 mm radius) to test the local effects of the irradiation with higher intensity on a smaller region.

Silicon detectors were never directly exposed to such high intensity proton beams before: in order to correctly evaluate the damage threshold, the number of proton bunches was gradually increased. The performance of the modules has been sistematically monitored after each pulse in order to ascertain the survival of the sensor and the electronics to that level of irradiation. Nevertheless, the effects are incremental, since the bunches are delivered subsequently on the same devices. In the first phase, the wide beam was used; after checking the survival of the detectors to the maximum intensity available for wide beams, a second phase was performed with narrow beams. Since it was possible to move the hit point of the beam by few mm, after the first phase the beam position was moved out of the irradiated region

in order to study the effect of narrow beams on a different portion of the modules.

The beam pulses used in the 2017 experiment include:

- wide beam (2 mm radius): 1, 4, 12, 24, 36, 72, 144, 288 bunches ($5 \cdot 10^{10}$ p/bunch)
- narrow beam (0.5 mm radius): 1, 12, 72, 288 bunches ($1 \cdot 10^{11}$ p/bunch)

The beam pulses used in the 2018 experiment include:

- wide beam (2 mm radius): 1, 4, 12, 24, 36, 72, 144, 288 bunches ($1 \cdot 10^{11}$ p/bunch)
- narrow beam (0.5 mm radius): 1, 12 bunches ($1 \cdot 10^{11}$ p/bunch)

In 2017, the 2 mm pulse with 288 bunches was repeated with higher intensity ($1 \cdot 10^{11}$ p/bunch); in 2018, it was repeated three times with the same intensity ($1 \cdot 10^{11}$ p/bunch).

Operations	2006 experiment	2017/2018 experiments
Beam line	Proton Synchrotron	Super Proton Synchrotron
Beam energy	24 GeV	440 GeV
Bunch intensity	$1 \cdot 10^{11}$ protons	$1 \cdot 10^{11}$ protons
Number of bunches	1 to 8	1 to 288
Bunch spacing	256 ns	25 ns
Beam profile	gaussian	gaussian
Beam direction	parallel w.r.t. modules	perpendicular w.r.t. modules
Module tested	Pixel	IBL pixel, ITk strip
Radiation hardness (TID)	50 MRad	250 MRad, 50 MRad
Established limit	$1.5 \cdot 10^{10}$ p/cm^2	$1 \cdot 10^{13}$ p/cm^2

Table 5.2: Summary of the operational parameters of 2006 and 2017/2018 experiments.

During the 2017 test beam, the experimental table with the ATLAS test box was installed downstream of the RotColl experiment [58] for the study of HL-LHC collimator robustness. The first day of operations was entirely dedicated to the ATLAS experiment, with the ATLAS team being the main user of the beam and setting its parameters. Then the ATLAS program was interrupted during the second phase, after 12 bunches, narrow beam. There was one week dedicated to RotColl operations, during which the ATLAS experiment was passively receiving a stream of secondary particles on the sensors. Finally one last day of the ATLAS experiment operations (delivering 72 and 288 bunches, narrow beam). The 2018 beam time was entirely devoted to the ATLAS experiment and the experimental program was completed in one night of operations.

Module	Total size	Sensor type	Sensor thickness	Chip type	Channel (Pitch)	Maximum dose
2017 test						
IBL	2×2 cm^2	n-in-p, 3D [59]	230 μm	FE-I4 [60]	26680 (50×250 μm^2)	250 MRad
ITk	1×1 cm^2	n$^+$-in-p, ATLAS12 [61]	320 μm	ABC130 [62]	104 (74.5 μm)	35 MRad
2018 test						
IBL	2×4 cm^2	n$^+$-in-n, planar [63]	200 μm	FE-I4 [60]	2×26680 (50×250 μm^2)	250 MRad
ITk	0.7×2.6 cm^2	n$^+$-in-p, PTP [61]	320 μm	ABC130 [62]	64/128 (77 μm)	35 MRad

Table 5.3: Summary of the modules characteristics used in 2017 and 2018 tests.

5.3 Devices

The HiRadMat test beam campaign started with the objective to test ITk pixel and strip detectors components. A first test was performed in 2017 with two available IBL pixel modules and one ITk strip module. It was expected to have ITk pixel modules in early 2018, therefore a second test was planned at the HiRadMat facility in 2018. Unfortunately the ITk pixel modules production suffered some delays, it was therefore decided to use a different IBL pixel module in the 2018 test beam, along with two ITk strip modules. A detailed description of the IBL and ITk strip devices is presented below. Details on the performed measurements and results for IBL pixels are presented in the following Sections. ITk strip modules measurements are out of the scope of this thesis: a complete overview of the experiment is going to be published. The specifications of the devices, in terms of modules, sensors and chips properties, are resumed in Table 5.3.

5.3.1 IBL pixels

In 2006, a pixel module from the initial Pixel detector was tested [56]. The Pixel detector [32] has been designed to face a Total Ionizing Dose (TID) of 50 MRad (expected at 300 fb^{-1}), a NIEL of $1 \cdot 10^{15}$ 1 MeV n$_{eq}$ cm^{-2} and a peak luminosity of $1 \cdot 10^{34}$ cm^{-2} s^{-1}. The Pixel module is made of planar $n{-}in{-}p$ sensors bump-bonded to FE-I3 read-out chips.

The new generation of ATLAS pixel modules developed for the IBL, at least a factor 5 more radiation-hard [1] than the pixel modules used in the 2006 test, has been tested in 2017 and 2018 experiments. The Insertable B-Layer has been built to sustain higher radiation levels, up to a NIEL of $5 \cdot 10^{15}$ 1 MeV n$_{eq}$ cm^{-2} and a dose of 250 MRad. In the IBL, two different silicon sensor technologies have been used: planar $n^+ - in - n$ (Figure 3.5, left) and 3D with passing through columns (Figure 3.5, right), bump-bonded to FE-I4 read-out chips [60]. The IBL planar module has the double size of a 3D module and it is made by two FE-I4 read-out chips (see Figure 5.2). In the HiRadMat test beam, two IBL modules with 3D silicon sensors and one IBL module with planar sensor have been tested in 2017 and 2018,

[1] This was the minimum requirement from the IBL TDR [64]. Some IBL modules have been irradiated with a 25 MeV proton beam to an estimated TID of 750 Mrad [64].